# QUANTITATIVE CHARACTERISATION OF FORCES

# AND FIELDS IN A MAGNETIC TWEEZERS

# INSTRUMENT

by

Michelle S.M. Lee

B.Sc., McMaster University, April 2005

THESIS SUBMITTED IN PARTIAL FULFILLMENT

OF THE REQUIREMENTS FOR THE DEGREE OF

MASTER OF SCIENCE

IN THE DEPARTMENT

OF

PHYSICS

© Michelle S.M. Lee 2007

SIMON FRASER UNIVERSITY

Fall 2007

# APPROVAL

**Name:** Michelle S.M. Lee

**Degree:** Master of Science

**Title of Thesis:** Quantitative Characterisation of Forces and Fields in a Magnetic Tweezers Instrument

**Examining Committee:** Dr. Jenifer Thewalt (Chair)

---

Dr. Nancy R. Forde (Senior Supervisor)

---

Dr. David Boal (Supervisor)

---

Dr. Michael Hayden (Supervisor)

---

Dr. John Bechhoefer (Internal Examiner)

**Date Approved:** November 28, 2007

# Declaration of Partial Copyright Licence

The author, whose copyright is declared on the title page of this work, has granted to Simon Fraser University the right to lend this thesis, project or extended essay to users of the Simon Fraser University Library, and to make partial or single copies only for such users or in response to a request from the library of any other university, or other educational institution, on its own behalf or for one of its users.

The author has further granted permission to Simon Fraser University to keep or make a digital copy for use in its circulating collection (currently available to the public at the "Institutional Repository" link of the SFU Library website <www.lib.sfu.ca> at: <http://ir.lib.sfu.ca/handle/1892/112>) and, without changing the content, to translate the thesis/project or extended essays, if technically possible, to any medium or format for the purpose of preservation of the digital work.

The author has further agreed that permission for multiple copying of this work for scholarly purposes may be granted by either the author or the Dean of Graduate Studies.

It is understood that copying or publication of this work for financial gain shall not be allowed without the author's written permission.

Permission for public performance, or limited permission for private scholarly use, of any multimedia materials forming part of this work, may have been granted by the author.   This information may be found on the separately catalogued multimedia material and in the signed Partial Copyright Licence.

While licensing SFU to permit the above uses, the author retains copyright in the thesis, project or extended essays, including the right to change the work for subsequent purposes, including editing and publishing the work in whole or in part, and licensing other parties, as the author may desire.

The original Partial Copyright Licence attesting to these terms, and signed by this author, may be found in the original bound copy of this work, retained in the Simon Fraser University Archive.

Simon Fraser University Library
Burnaby, BC, Canada

# Abstract

Magnetic tweezers are used in single-molecule manipulation experiments to probe systems, such as supercoiled DNA, and mechanisms of molecular motors, such as topoisomerases. A superparamagnetic bead is subjected to an external magnetic field to exert sub-pN to pN forces and torque on a tethered molecule. In this thesis, we compare the calculated forces acting on a bead to experimental forces determined by stretching a single dsDNA molecule and discuss factors which account for the differences between these two curves.

The relevant magnetic fields are calculated and experimentally characterised for a rare-earth magnet pair. The induced magnetic moment, alignment and rotation of the superparamagnetic bead are discussed. With knowledge of the field and the moment of the bead, the expected force on a bead is calculated. We present the details of our data analysis along with key corrections, which account for instrumental drift and spherical aberration when using an oil-immersion objective.

# Acknowledgments

First and foremost, I would like to thank the "boss", Nancy, for her guidance, unyielding patience, and thorough grasp of the English language. Thank you also to all members of the Forde lab, past and present, for making the sun shine inside. I am especially grateful to Yi Deng, Astrid van der Horst, and Benjamin Downing for intellectually-stimulating and, sometimes, just plain silly conversation. I must also acknowledge Marieke Berga who deserves an award for teaching molecular biology lab techniques to a physics kid.

Thank you to Mike Hayden for scientific discussion, project-altering suggestions, and use of his lab's Hall probe. I would also like to convey my deep appreciation to Vic Allen for his machining know-how and generally pleasant disposition.

Thank you to my family who consistently provides me with other things to think about. Furthermore, I am eternally indebted to my friends whose laughter I could not do without. And to my climbing partners: you rock!

Finally, thank you to the beauty of nature and the pursuit of science. May they humble us forever.

> "We shall not cease from exploration, and the end of all our exploring will be
> to arrive where we started and know the place for the first time." ~T.S. Eliot

# Contents

# List of Tables

# List of Figures

# Chapter 1

# Introduction

Within the cramped volume of a cell, molecules are constantly being pushed and pulled while chains are wound and unwound. These growth and maintenance processes are made possible by enzymes and molecular motors which exert forces and torques on molecules. It is one of the goals of single-molecule biophysics to accurately probe these systems, independent of bulk interactions, and uncover the underlying stochastic phenomena.

Many techniques have been developed to study single molecules by applying biologically relevant forces in the range of femtoNewtons to nanoNewtons [1] (Fig. 1.1). When pulling with the atomic force microscope (AFM), a single molecule is tethered between the cantilever and a surface. The deflection of the cantilever provides a measure of the force being applied to the molecule, which can be as high as nanoNewtons [1]. The forces applied by the optical tweezers depend on the stiffness of the optical trap and range roughly from 1 pN to 100 pN [1]. In a typical optical tweezers apparatus, a molecule is specifically tethered between a bead whose position is controlled externally and a bead trapped at the focal point of an infrared laser. The force exerted on the molecule can be determined from the offset of the trapped bead from the centre of the trap. Both AFM and optical tweezers are capable of generating relatively high forces, but generally have poorer sensitivity in the low force regime. Together they span a wide range of biologically relevant forces, but do not extend into the sub-pN range.

The magnetic tweezers instrument tackles this force range deficiency and also provides easy access to the rotational degree of freedom of the tethered molecule. The magnetic tweezers instrument constructed in this thesis is intended to probe a single molecule specif-

1
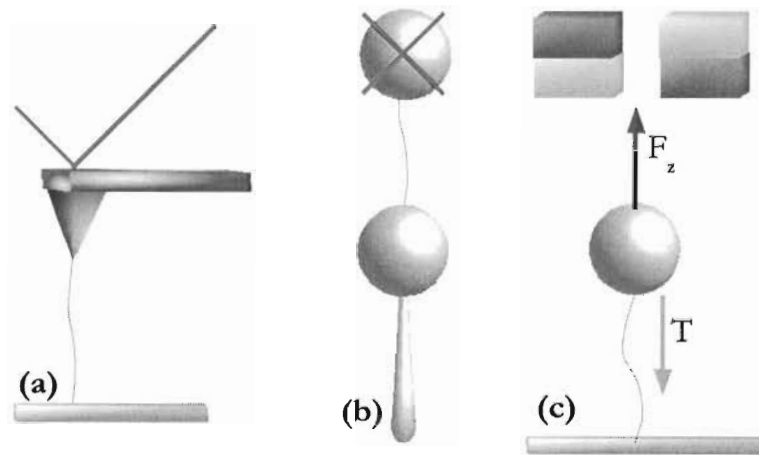
Figure 1.1: A schematic comparison of single molecule manipulation techniques: (a) atomic force microscope, (b) optical tweezers, and (c) magnetic tweezers

ically tethered between a superparamagnetic bead and surface. Interactions between a magnet pair and the bead generate an upwards force which pulls the bead away from the surface. The bead is 'trapped' because it is in dynamic equilibrium between the force from the magnets and the tension in the molecule. This set-up is better suited to obtain high resolution sub-pN pulling forces than either the AFM or optical tweezers.

We have developed the typical passive force clamp version of the magnetic tweezers using permanent magnets, which is similar to the instrument constructed in [2]. A force perpendicular to the chamber surface is applied to a superparamagnetic bead and its position is measured as a function of time. Another common version of the instrument, the position clamp, is designed to maintain a constant position of the bead by changing the applied force. This requires active feedback, which is most easily attained with electromagnets [3, 4]. Variations of these two designs have given rise to devices that apply forces parallel to the surface [5, 6], have three-dimensional control of magnetic particles [7], and apply a constant force over a large area [8, 9], to name just a few.

## 1.1 The Magnetic Tweezers: a tool with many applications

Magnetic tweezers have induced and measured the mechanical responses of different samples over a wide range of length scales. The main advantage of magnetic tweezers over many other systems is their ability to act as a passive force clamp. That is, the force acting on a micron-sized bead does not change appreciably under thermal fluctuations and only changes when the magnets are moved macroscopically.

The magnetic tweezers instrument has been used in microrheology studies to investigate elastic properties of the cell since the 1950s. F.H.C. Crick prepared cells in which magnetic particles had been phagocytosed and applied "twisting, dragging and, prodding" to the internal environment of a cell [10]. Since then, higher-resolution techniques have been developed to study the mechanics of the cell membrane and cytoskeleton with magnetic beads bound to membrane proteins or incorporated into the internal actin network, for example [11, 12].

Despite its historical and continued use on micron-scaled samples, the magnetic tweezers instrument has gained most of its recognition from studies involving single-molecule manipulation. It has been a very useful tool because in addition to generating a pulling force, the magnetic tweezers instrument is also able to apply positive and negative torques to a tethered molecule. This is possible because the bead maintains a preferred direction in the presence of the magnetic field from the magnet pair. Supercoiling a molecule is as easy as rotating the magnets.

These manipulation abilities are far-reaching as they provide access to the stretch and twist regions of the phase diagram of molecules which have have a natural chirality. Magnetic tweezers can probe the physical properties of a single molecule, such as its elasticity, torsional rigidity and pitch [13, 14]. Force-extension curves have been generated in which a chain of nucleic acids (such as ssDNA, dsDNA, and RNA) is stretched and the extension response of the molecule is measured [15, 16]. Plectonemes and P-, B- and L-DNA structures have been inferred from the torque-extension curves produced when supercoiled DNA is held at a fixed stretching force [13, 17]. There are also many recent mechanical response results involving magnetic tweezers, such as the counter-intuitive observation that overwinding DNA while stretched increases its extension [18, 19]. Another current and popular application involves the torsional manipulation of chromatin to aid in the understanding of

nucleosome-DNA dynamics [20].

Although magnetic tweezers have been used mainly for single-molecule DNA-based studies, they are not restricted to studying just the response of nucleic acids. $F_1$-ATPase is an enzyme responsible for the hydrolysis of ATP in cells and has a structure which resembles a rotary motor. Experiments involving magnetic tweezers have shown that the motor also operates in reverse. ATP can be synthesized from ADP and a phosphate group by mechanical rotation of the appropriate subunit of the enzyme in the direction opposite to the one causing hydrolysis [21].

Another group of experiments focuses on understanding the mechanism of topoisomerases, a family of enzymes responsible for changing the degree of supercoiling in DNA by passing one strand through another. Magnetic tweezers have been used to investigate the enzymes' processivity and effective step size, and the dependence of the activity rate on ATP concentration and degree of stretch and supercoiling of the DNA [22, 23]. A comprehensive model for the physical mechanism for the type II topoisomerase, *E. coli* DNA gyrase, has since been proposed [24].

The above discussion highlights only some of the research being conducted with magnetic tweezers, and is by no means an exhaustive list. From this selection, it is clear that this technology will continue to have many applications in the future.

Development of our magnetic tweezers instrument is motivated by experiments to pull and twist a single molecule of collagen, the predominant structural protein in vertebrates. At its molecular level, collagen is a non-globular protein composed of three α-chains wound together to form a triple helix. A single molecule is ∼300 nm in length and ∼1.5 nm in diameter. In our experiments, we hope to determine the rigidity of the molecule through force-extension measurements, probe the unfolding and refolding processes of the triple helix by applying torque, and begin to assemble the force-torque-temperature phase diagram of collagen at the single-molecule level.

**Our approach**

Although the basic components of magnetic tweezers are the same from instrument to instrument, the approach to an experiment and analysis technique employed by different groups varies. Some groups have chosen to calibrate the force applied to the bead such that during a measurement the force is defined by the position of the magnet pair [2]. In prin-

ciple, force calibration is an appropriate technique that saves time during a measurement, but due to differences in magnetic moments among beads we have chosen not to implement this method. In our instrument, we are simultaneously making measurements of both the force applied to the bead and the extension of the molecule while holding the magnets at a fixed height.

In the literature, determination of the force acting on a magnetic bead has been performed in two ways. The first involves flow [3, 8]. In this technique, the position of an untethered bead is balanced between the magnetic force and the Stokes' drag force generated from flow of the medium surrounding a sphere. This technique is not easily accessible to our instrument as it requires application of controlled flow in the sample chamber and imaging of the direction parallel to the applied force. Our instrument images bead displacements most easily in the plane transverse to the applied force. The second method relates the Brownian motion of a tethered bead to the pulling force. We rely on this relationship to perform our measurements and describe it in detail in Chapter 4.

The first application of magnetic tweezers to single-molecule experiments occurred in 1992 by Smith, *et al.* [5], and it has since become an accepted technique for applying and measuring forces and torques. Despite the common use of the technique, a comprehensive characterisation of the instrument has yet to be published. While more sophisticated designs of electromagnets have been developed [3, 4], advances in the design and understanding of the permanent magnet versions of the magnetic tweezers have been overlooked. The origin of the magnetic "trap" has been explained briefly [3, 25], but a thorough review of the physical principles and analysis involved in the use of magnetic tweezers remains unavailable. This thesis attempts to address some of these issues and provide information specific to our instrument.

## 1.2   Thesis organization

Chapter 2 discusses the components of a magnetic tweezers instrument, the abilities of the software interface and details about the single-molecule sample preparation, including a section describing the superparamagnetic beads used.

The bead height calibration and measurement modes for video microscopy required to determine the extension of the molecule are explained in Chapter 3. This chapter also

presents the details of two key corrections required in the analysis.

Quantitative examination of the magnetic field and pulling force acting on the bead tethered by dsDNA are carried out in Chapter 4 for two different configurations of the magnet pair. Calculated magnetic fields are experimentally verified by Hall probe measurements. Expected forces on an *average* bead are compared to observed forces on a real bead. Double-stranded DNA (dsDNA) stretching data, taken by the magnetic tweezers and fit to a mathematical interpretation of the worm-like chain model for semi-flexible polymers, is presented. Experimental implications of multiple tethers and tips to increase the probability of acquiring a single tether are provided. Also included are criteria for aligning the magnets with respect to the rotational and optical axes.

The final chapter provides a discussion of future work, including possible improvements to the system, and a short summary of the thesis.

# Chapter 2

# Instrumentation and Sample

## 2.1 Apparatus

The magnetic tweezers instrument is built on an inverted light microscope (Nikon TE2000S) known for its superior stability. Figure 2.1 shows the side view of the apparatus, and Appendix A provides further details about the components. To maximize the accessible area above the sample stage, the condenser has been replaced by an adapted Koehler Illumination pillar (see next paragraph). A pair of rare-earth magnets is attached to a motorized rotational stage whose rotational axis is aligned with the optical axis of the microscope. The rotational stage is secured to a motorized linear positioner which controls the height of the magnets from the sample chamber. The objective lens is a 1.4 NA, 100x oil-immersion Plan Apochromat lens. Its height is controlled via the fine focus adjustment knob, which is fitted with a motorized Z-axis Focus Drive with a step size of 0.2 $\mu$m. A CCD camera is used to digitize a 38 $\mu$m x 30 $\mu$m area of the microscope's field of view. The entire apparatus rests on a vibration isolated workstation. In addition to the proximity of the magnets to the sample chamber, the orientation of and gap in between the magnet pair also determine the force exerted on a tethered molecule. A quantitative discussion of these factors is presented in Chapter 4.

In a microscope, the condenser lens typically is involved in smoothing the light from a non-uniform source, such as a filament, into a beam of uniform intensity collimated light (Koehler illumination). Koehler illumination is required to maximize the contrast and resolution of the sample image. To achieve this type of illumination in our apparatus, we have

**Legend**

1  100W lamp house
2  12V halogen light bulb
3  filters: neutral density, neutral colour
        balance, heat absorbing
4  adapted Koehler pillar
5  red filter
6  linear positioner
7  rotational stage
8  magnet holder
9  rare-earth magnets
10 sample chamber
11 XY stage
12 100x oil-immersion objective
13 microscope arm
14 CCD camera
15 motorized controller of fine focus knob

Figure 2.1: Schematic of the magnetic tweezers instrument, side view

implemented an adapted Koehler pillar downstream of the microscope light source (Fig. 2.2). The light from the 100W Halogen bulb is directed through a concave lens of focal length 25 mm. An adjustable iris diaphragm is located at a distance just greater than 25 mm downstream where the diameter is set to encompass the bright focal point ($d \approx 2.5$ mm). Another 25 mm downstream, an identical lens is used to capture the diverging light and produce a nearly uniform, collimated beam.
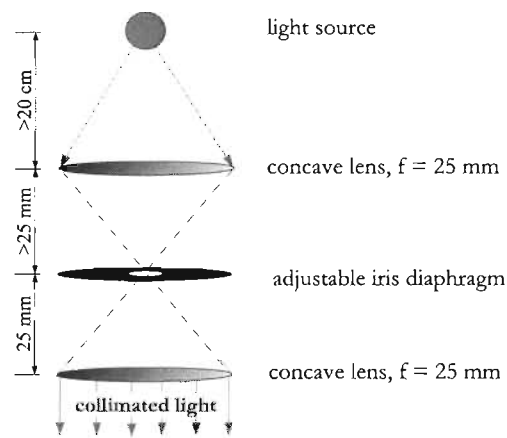


Figure 2.2: Adapted Koehler illumination pillar takes non-collimated light from the microscope light source and produces a collimated, uniform beam to illuminate the bead. This figure is not drawn to scale.

## 2.2  Software interface

A customized LabVIEW program provides the software interface to control the instrument. This program also activates the analysis which determines the (x,y,z) position of the bead.

Figure 2.3 shows the program's visual interface, with functional blocks labeled 1 through 6. Block 1 controls the three motorized stages (linear positioner, rotational stage and objective height). The on/off status, position (linear and rotational), rate of motion and Home location of each stage can be controlled and read out. The ABORT button signals the equipment to stop all movement. Block 2 specifies the mode of operation and other tasks for the program to perform. A pulldown menu allows the user to choose among Normal (idling), Calibration (live or from saved images), Measurement (live or from saved images), Drift Measurement, and Magnetic Field Strength Measurement (with the use of a Hall Probe). Selection of the 'Movie' button will cause each camera frame to be saved as a JPEG. When the 'Analyze' button is enabled, the program will calculate the (x,y,z) position of a bead in real time. The z position will only be meaningful if a calibration of that particular bead has already been conducted; details are presented in Chapter 3. Block 3 displays the camera image. When 'Analyze' and the position hand tool are selected, double clicking within a few pixels of the centre of the bead will initialize the centre-finding subroutine. Block 4 displays the output of relevant, calculated quantities of the program. Some of these will be discussed in later chapters. Block 5 provides controls for the camera such as shutter speed, and for file saving which allows the user to specify the root name of any output files. Each tab in Block 6 is responsible for controlling certain variables in each mode. For example, the 'Calibration' tab takes input for the number of steps in the calibration, the number of images in each step to average over, and the change in objective height for each step. The 'Centre' tab tracks the centre of the bead on an (x,y) graph which is useful when aligning the magnets with respect to the optical axis. The LabVIEW program and subVIs have been written specifically to suit the needs of this apparatus.

## 2.3 Sample

To test our system, initial experiments using this apparatus involve DNA because its mechanical response has been well characterised by many different techniques [5, 15, 26, 27, 28, 29, 30] and can therefore serve as a measurement standard. Although an experiment is performed on a single molecule, we assemble many tethered molecules during the preparation of each sample. The biomolecules are probed within a flow chamber to which they are tethered between the surface of the chamber and superparamagnetic beads via ligand-
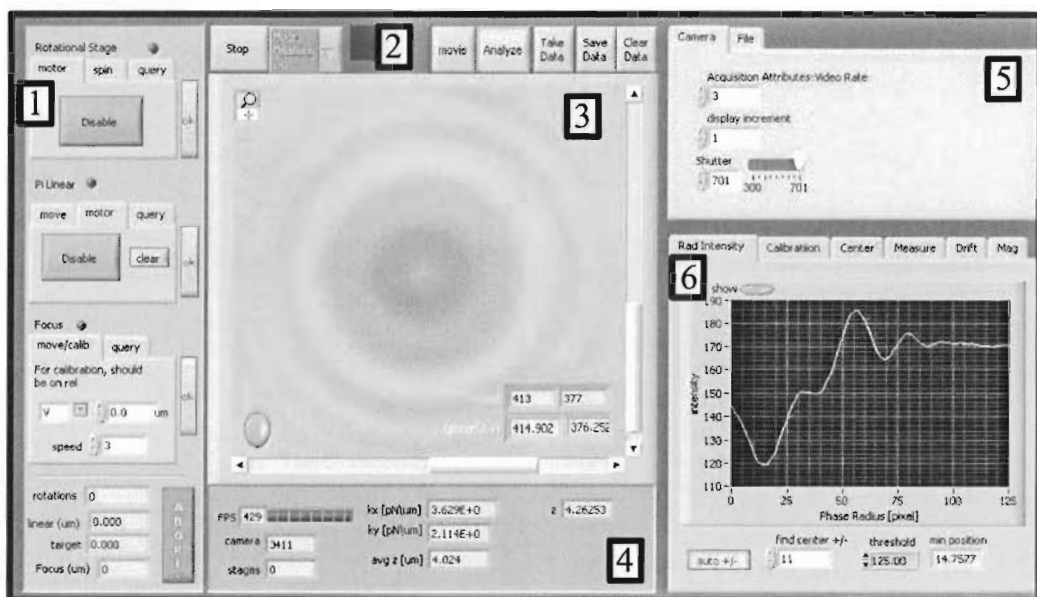
Figure 2.3: Front panel of the LabVIEW software interface program. See Section 2.2 for details.

receptor interactions (Fig. 2.4). The flow chamber sits directly above the inverted microscope objective lens with the magnet pair some distance above the chamber. The sample can be subdivided into three main components: labeled DNA, the flow chamber, and the superparamagnetic bead. Once differentially labeled DNA is constructed, it can be chemically tethered to a surface and to a superparamagnetic bead. We first describe the DNA, then the flow chamber which provides the stationary surface on which to attach the DNA. Following that, the superparamagnetic bead will be discussed in detail.

## 2.3.1 Labeled DNA

For typical single-molecule DNA studies, connections must be made between each end of the DNA and a surface. In general, each end of the DNA is *labeled*, or coupled to a distinct ligand, and the surface is labeled with the complementary receptor. Note that the terms 'ligand' and 'receptor' are used loosely and refer generally to the molecular connections that attach an end of DNA to a surface. These ligand-receptor sets are structurally complementary molecules that have a strong noncovalent affinity for each other.
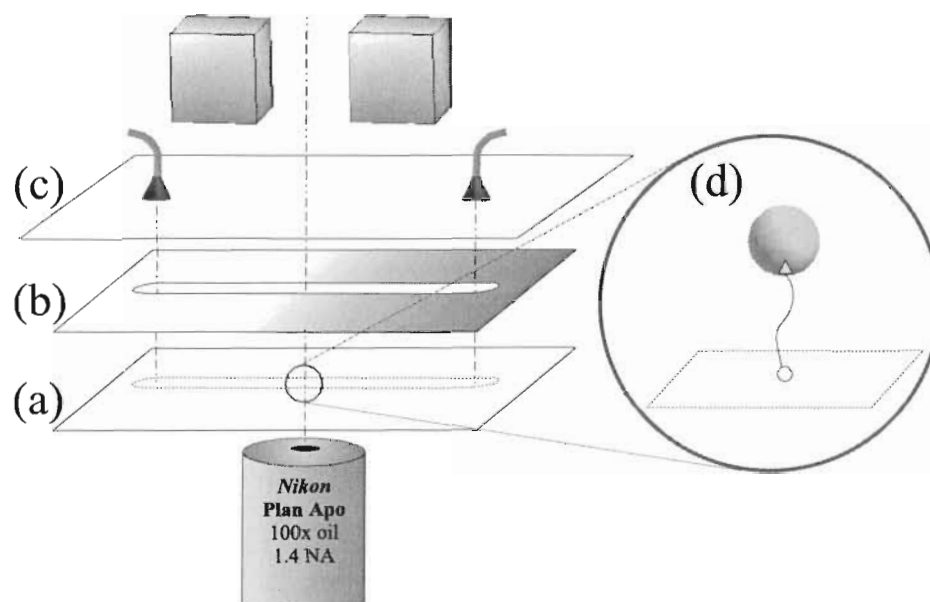
Figure 2.4: The sample chamber, located between the magnets and objective lens, provides a stable aqueous environment for the biomolecule to be probed and is composed of three parts (a-c). (a) A #1 cover glass provides a surface to which the molecule can be tethered via receptors, such as the streptavidin protein. (b) Double-sided masking tape with a slot provides a thin reservoir for fluid. (c) A strip of transparency film with tube attachments for buffer exchange functions as the capping layer of the chamber. When sandwiched together, these three layers provide an enclosed volume ($\sim$50 $\mu$L) in which (d) the molecule can be tethered between a superparamagnetic bead and the surface via molecular connection points indicated by the triangle and circle. This diagram is not drawn to scale.

The formation and dissociation of the bond between ligand and receptor is a stochastic process which requires overcoming an energy barrier. So, the pulling force required to rupture the interaction, $F_{rup}$, is statistical and cannot be predicted exactly [31]. However, faster loading rates usually yield a higher $F_{rup}$ due to nonequilibrium loading conditions. One example of a widely used ligand-receptor pair is the biotin-streptavidin system, one of the strongest noncovalent interactions presently known. Digoxigenen (DIG) and anti-digoxigenin (antiDIG) form another common pair. Once bound, these sets of bonds have a very low probability of dissociating at the forces exerted by the magnetic tweezers (0.1 to 10 pN). The biotin-streptavidin bond will likely remain bound up to forces of 100 pN, while 50 pN is the usual threshold for the DIG-antiDIG bond [32]. For comparison, a covalent bond requires nanoNewtons of force before the probability of rupturing is significant [33].

Streptavidin is an eight-stranded β-barrel protein that has four biotin binding sites [34]. Biotin, or vitamin $B_7$, can be covalently linked by a short chain to a nucleotide. The linking strand is an organic chain which acts as a spacer to allow incorporation of the labeled nucleotide into the DNA sequence. Bio-11-dCTP, a biotin-labeled cytosine, can be integrated into the DNA sequence in lieu of dCTP, thus providing a molecular connection between the DNA molecule and surfaces coated with streptavidin. Digoxigenin-14-dUTP is also commercially available for coupling to antiDIG-coated surfaces.

AntiDIG is the antibody which specifically targets DIG, a steroid molecule. AntiDIG is commercially available and can be easily crosslinked to surfaces already coated with Protein G, an immunoglobulin-binding protein [35].

**Differentially labeled DNA**

In this project, differentially labeled DNA was prepared as described in [36]. This protocol yields a 3.96-$\mu$m-long piece of double-stranded DNA with a different label on each end (Fig. 2.5). The positions of the labels are known to within one basepair, and so the contour length can be calculated with minimal uncertainty.

A protocol for preparing multiply labeled DNA for experiments requiring torsional constraint is presented in Appendix B.
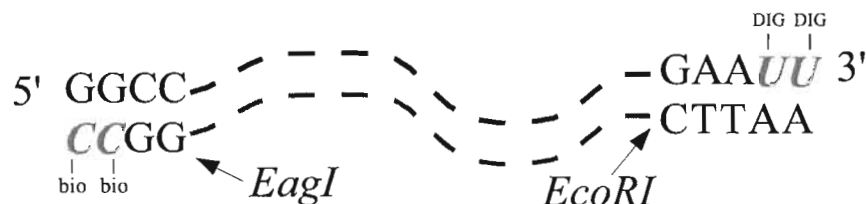
Figure 2.5: Differentially labeled DNA consists of an unlabeled length of DNA with two sticky ends which have been filled in with *labeled* and unlabeled nucleotides. Note that DIG-14-dUTP replaces T, as the complementary base pair of A. The sticky ends are the product of the endonucleases *EagI* and *EcoRI*. The dashed lines represent the length of unlabeled dsDNA.

## 2.3.2 Flow chamber

The flow chamber contains the DNA-bead complex in an aqueous medium and provides a surface to which the DNA can be tethered (see Figure 2.4). The flow chamber volume is minimized to limit the amount of DNA and number of beads required for each experiment. With the current design, the chamber holds approximately 50 $\mu$L of liquid while providing about 150 mm$^2$ of surface area on which to bind the DNA.

There are three main layers of the flow chamber, as illustrated in Figure 2.4. The bottom is a streptavidin-coated #1 cover glass (thickness $\sim 170\mu$m) which provides the molecular connection for a biotin-conjugated DNA strand to the slide surface. Details of this coating procedure are provided in the next paragraph. The middle layer consists of a strip of double-sided masking tape (thickness $\sim$0.3 mm) approximately the size of the cover glass. A 3 mm x 50 mm slot is cut along the centre of the long axis of the tape to serve as a reservoir when the tape is applied to the cover glass. The top and final layer is a piece of transparency film (for overheads) that acts as a cover providing an optically transparent seal for the reservoir. Two holes punctured at appropriate locations in this third layer serve as input and output junctions to thin PE10 tubing (Intramedic$^{TM}$, 427401). Each tube is connected to a syringe which allows fluid to be exchanged in the chamber. Note that because of the fragility of the chamber, it is always better to pull the fluid through the output syringe than to push on the input syringe.

Our sample preparation involves adhering biotin-BSA (bovine serum albumin) to the

cover glass and binding streptavidin to this complex [37]. BSA is electrostatically held to the glass surface providing a simple method of coupling molecules to the chamber [38]. First, BSA-biotin (Sigma, A8549) is dissolved in T50 buffer (10 mM Tris, pH 8.0, 50 mM NaCl) to a concentration of 1 mg/mL. Then 75 $\mu$L of this mixture is incubated on a clean cover glass for 30 minutes. After inactivating the remaining exposed surface with SuperBlock$^{TM}$ (Pierce, 37535) for 1 hour, the slide is washed for five minutes in TBS-Tween. The wash step is repeated another two times. 5 mg of streptavidin (Molecular Probes, S888) is dissolved in 1.66 mL NaOAC. This mixture is diluted 1:1000 in TBS-Tween. About 30 $\mu$L of the diluted solution is added to the cover glass surface and is incubated for 1 hour to allow it bind to the BSA-biotin already adhered to the cover glass. This technique takes advantage of the multiple biotin-binding sites in streptavidin. There is a noticeable decrease in the surface tension of the incubating solutions where the cover glass has been coated with BSA. The slide is then washed three times for five minutes with TBS-Tween and then another two times for five minutes with TBS to remove any Tween detergent. Once dried, the slide is ready to be assembled into a flow chamber.

It is possible to make a large number of coated slides for later use if they are dried after the last washing steps and refrigerated (4 °C). The amount of reagent can be minimized if a mask is used to contain the incubating surfaces. Double-sided tape can serve as the mask, although it should be carefully replaced by a new, dry piece before the chamber is assembled.

### 2.3.3 Superparamagnetic bead

A force acts on a superparamagnetic bead to stretch DNA in the magnetic tweezers. There are two key characteristics about the superparamagnetic beads we use that make them useful for single-molecule research: (1) the surface of the beads can be covalently linked to antiDIG; and (2) the bead can be magnetised by an external field but does not retain any net magnetic moment when the field is removed.

**Labeling the beads**

The labeled DNA constructed for our experiments is differentially end-labeled with biotin and DIG. Attachment of the DNA to the superparamagnetic bead requires that the bead

Table 2.1: Physical details about Dynabeads$^{TM}$ Protein G superparamagnetic beads [39]

| type | Dynal M270 |
|---|---|
| coating | Protein G (Dynal 100.03) |
| diameter | $2.8 \pm 0.2\ \mu$m |
| density (dried) | 1.6 g/cm$^3$ |
| approximate mass | 20 pg/bead |
| % mass from iron content | 17 |
| iron domain size | <30 nm (very polydisperse) |
| minimum # of iron domains | 20,000/bead |

be coated with antiDIG. We use an established protocol to crosslink antiDIG to Protein G beads [35].

Superparamagnetic beads are commercially available with a number of different surface coatings, including Protein G. The following is a description of the protocol we used to coat our Dynabeads$^{TM}$ Protein G superparamagnetic beads (3% w/v of M270, Dynal) with antiDIG. A physical description of this bead is given in Table 2.1. Due to their magnetic content, the beads will aggregate in the presence of an external magnetic field, so these reactions must be performed in a zero or very weak field, unless otherwise stated. First, 1 mL of the beads are concentrated with a magnet, the supernatant is removed and the beads are washed with PBS buffer, pH 7.4. The beads are trapped again, and the supernatant is removed. The beads are then resuspended in Ab X-linking buffer (100 mM NaCl, 100 mM Na$_2$HPO$_4$) to make a 5% w/v solution (600 $\mu$L). 36 $\mu$L of antiDIG solution and 18 $\mu$L of dissolved DMP (Fluka, 80490) are added. The antiDIG solution is prepared by dissolving 200 $\mu$g of polyclonal sheep antiDIG (Roche, 11333089001) in 200 $\mu$L of PBS buffer pH 7.4. The DMP crosslinking solution should be prepared immediately before use by combining 500 $\mu$L of Ab X-linking buffer with 25 mg of DMP. After tumbling the bead mixture for 1 hour, the beads are concentrated with a magnet and the supernatant is removed. For a 5% w/v solution of antiDIG-coated superparamagnetic beads, the beads are resuspended in 600 $\mu$L of PBS pH 7.0. The beads are now ready to be incubated with DIG-labeled DNA. For long-term storage, the buffer should include 0.2% NaN$_3$ to inhibit bacterial growth.

## Superparamagnetism

The superparamagnetic bead is a porous polystyrene mesh whose nonuniformly distributed empty spaces have been impregnated with nanometer-sized $\gamma Fe_2O_3$ and $Fe_3O_4$ ferrimagnetic particles [39]. The atomic components of ferrimagnetic materials have magnetic moments which are antiparallel. The magnitude of the moments are unequal and give rise to permanent magnetisation. Each particle in the bead is less than 30 nm in diameter, which is the maximum size of a single magnetic domain. The surface of the bead is sealed to prevent direct interactions between the iron oxide and later surface chemistry that may be used. Each iron oxide domain will find its equilibrium magnetic moment direction in the Néel relaxation time, $\tau = \tau_0 exp(\frac{KV}{k_BT})$ [40]. $\tau_0$ is the time constant ($\sim 10^{-9}$ s). $K$, the anisotropic energy of the particle, depends on the shape of the particle, temperature and the magnetic field to which it is exposed and is approximately $4 \times 10^4$ $J/m^3$ [40]. $V$ is the volume of the particle and $k_BT$ is the thermal energy. Therefore, an estimate of $\tau$ for these domain sizes ($\sim 10$ nm) is on the order of $10^{-5}$ s. For the time scale of our experiment, it can be assumed that each domain is always oriented along the field when present.

Superparamagnetic material has the characteristics of a paramagnet, namely that the material only magnetises in the presence of an external field. However, the physical origins of these phenomena are different. Paramagnetism arises from unpaired electrons in the atomic orbitals. Only weak interactions exist between the magnetic dipoles of atoms in these materials. An external field tends to align the dipoles resulting in an overall magnetic moment. When the field is removed, thermal fluctuations randomly orient the dipoles yielding no net moment. By contrast, superparamagnetic material is composed of weakly interacting, spatially separated ferrimagnetic or ferromagnetic single-domain particles. A domain is a collection of magnetic dipoles whose minimum energy configuration occurs when all the dipoles are oriented in the same direction. Furthermore, because the interaction of dipoles within a domain is stronger than thermal fluctuations, a nonzero magnetic moment of the domain is retained even in the absence of an external field. However, in the absence of an applied field, there is no directional correlation in magnetic moments of different domains. So, like the dipoles in paramagnets, it is the domains in superparamagnets that align in a field and randomly orient in the absence of a field. The bead used in these experiments is a matrix with spatially separated single-domain ferrimagnetic particles and

so can be considered superparamagnetic.

For simplicity, contributions from each ferrimagnetic domain can be calculated to yield a net magnetic moment of the bead. If there is no external field, the moment of each domain will point in a random direction resulting in a net magnetic moment of near zero. If an external field is applied, the non-uniform spatial and size distribution of the domains within the polystyrene beads yields a net dipole moment which is not necessarily located at the centre-of-mass of the bead.

Like a true paramagnetic material, the proportion of aligned domains of a superparamagnetic bead depends on field strength. The relationship between the induced magnetic moment and the applied external field is shown in Figure 2.6. This moment-field curve is characteristic of paramagnetic and superparamagnetic materials. At zero field, there is no net magnetic moment. There is no hysteresis because superparamagnetic (paramagnetic) materials retain no memory of the domain (dipole) orientation when the field is removed. If the field strength is increased from zero, the magnetic moment increases quickly until it reaches saturation. Saturation occurs when the applied field is strong enough to align all the magnetic domains in the bead. Above the saturation field, there can be no increase to the magnetic moment of the bead.

Due to the ability of proteins to bind to their surface and their capacity for induced magnetic moment, superparamagnetic beads have the ability to manipulate single molecules. Manipulation can occur in two ways: application of a stretching force and application of a torque. Briefly, the bead is pulled towards the magnet with a force that depends on the gradient of the inner product between the magnetic moment of the bead and the applied field. Because the DNA molecule is tethered between this bead and a fixed surface, the DNA also feels this force. A thorough explanation of the pulling force is discussed in chapter 4.

Magnetic tweezers are also able to apply torque to the tethered molecule. Torque is applied to a torsionally constrained molecule by rotating the bead, which can be accomplished by rotating the magnet pair in the xy plane. We assume that in the absence of thermal fluctuations and when viewed on the yz plane (parallel to field direction), the bead maintains a preferred orientation with respect to a magnetic field where the position of the net magnetic moment, $r_{net}$, is positioned directly above the tether point (Fig. 2.7). See Section 4.3.3 for a discussion on the difference between the bead's behaviour on the yz and xz planes.

To rotate the bead in the xy plane, an anisotropy in either the field or in the bead is
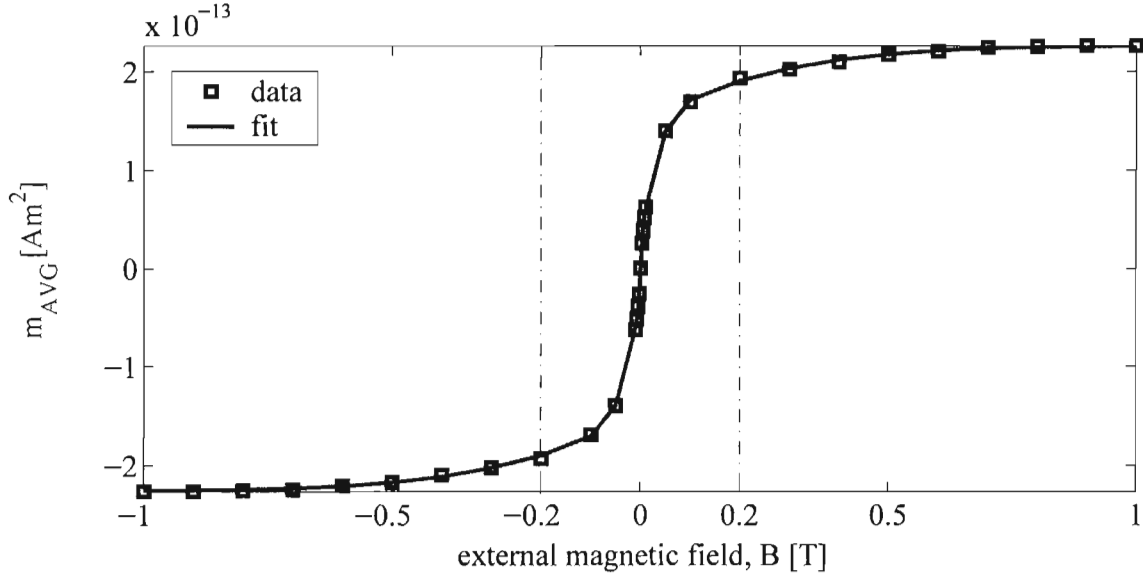
Figure 2.6: The magnetic moment of a bead, **m**, depends on the external magnetic field, **B**, in a nonlinear manner. Above **B** = 0.2 T, the moment can be considered saturated and, therefore, constant. In the current design of our instrument, we can access **B** from 0.02 T to 0.5 T. This curve has been calculated from data supplied by the manufacturer for the magnetic moment of a gram of dried beads, $\mathbf{m}_{bulk}$ as a function of external magnetic field, **B**: $\mathbf{m}_{bulk} = A + \sum \frac{a_i}{1+e^{-b_i \mathbf{B}}}$ ($A$ = -12.3 emu/g, $a_1$ = 7.708, $b_1$ = 5.39x10$^{-4}$, $a_2$ = 13.11, $b_2$ = 4.27x10$^{-3}$, $a_3$ = 3.79, $b_3$ = 4.12x10$^{-2}$; $a_i$ in [emu/g] and $b_i$ in [G$^{-1}$]). $\mathbf{m}_{AVG}$, the magnetic moment of a single bead on average, was calculated from $\mathbf{m}_{bulk}$ based on the density and volume of dried beads.

required, in addition to the dominant gradient in the z direction required for the application of vertical force. Here we discuss the effects of an inhomogeneous field in the xy plane. See Figure 2.8a to understand how a torque ($\tau$ = **r** x **F**) can act on a tethered superparamagnetic bead. We decompose the dipole moment into two components, located on opposite sides of the tether point and in the xy plane, since there is no displacement between the pivot point and position of the net dipole moment. A torque acts on the bead to keep it aligned with a field centred at $\mathbf{r}_{net}$ for gradients generated by our magnet pair of |**B**| along the x and y directions (Fig. 2.8b-e). So, the bead will rotate by maintaining alignment with the direction of the field between the magnet pairs.
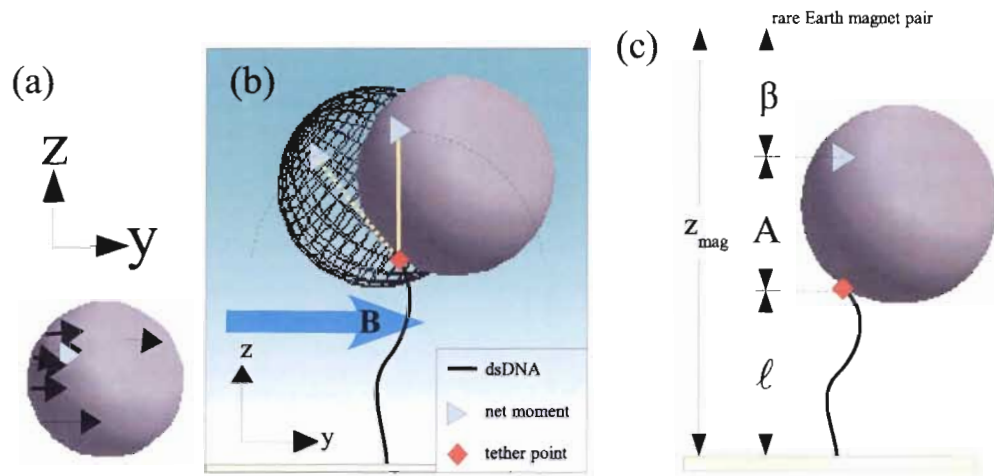
Figure 2.7: (a) The position of the net magnetic dipole (blue triangle), $\mathbf{r}_{net}$, can be calculated from the contributions of the magnetic moment of each ferrimagnetic particle within a bead (black arrows). The anisotropy of magnetic particle distribution and displacement of $\mathbf{r}_{net}$ from the centre of the bead are exaggerated for effect. (b) A superparamagnetic bead is tethered by DNA to a surface. The $\mathbf{B}$ field points along the y axis, and has a gradient along the z axis, with $\mathbf{B}$ increasing with z. The energy of the bead is $E = -\mathbf{m} \cdot \mathbf{B}$. For superparamagnetic material, $\mathbf{m}$ and $\mathbf{B}$ are always parallel. The equilibrium orientation of the bead occurs when $E$ is minimized. $E_{min}$ occurs when $|\mathbf{m}||\mathbf{B}|$ is maximized. This happens when $\mathbf{r}_{net}$ is in the strongest $\mathbf{B}$ it can access. Since the bead will pivot about the tether point, the equilibrium orientation occurs when $\mathbf{r}_{net}$ is positioned directly above the tether point. The vector between the tether point and $\mathbf{r}_{net}$ (green line) is fixed in length and should remain parallel to the z axis. (c) This schematic shows the relationship between relevant lengths in our system (not drawn to scale). $z_{mag}$ is the distance from the chamber surface to the magnets (typically mm). $\beta$ is the distance between $\mathbf{r}_{net}$ of the bead and the magnet pair (typically mm). A is the constant distance between the tether point and $\mathbf{r}_{net}$ ($\sim \mu$m). $\ell$ is the DNA extension (typically $\mu$m).
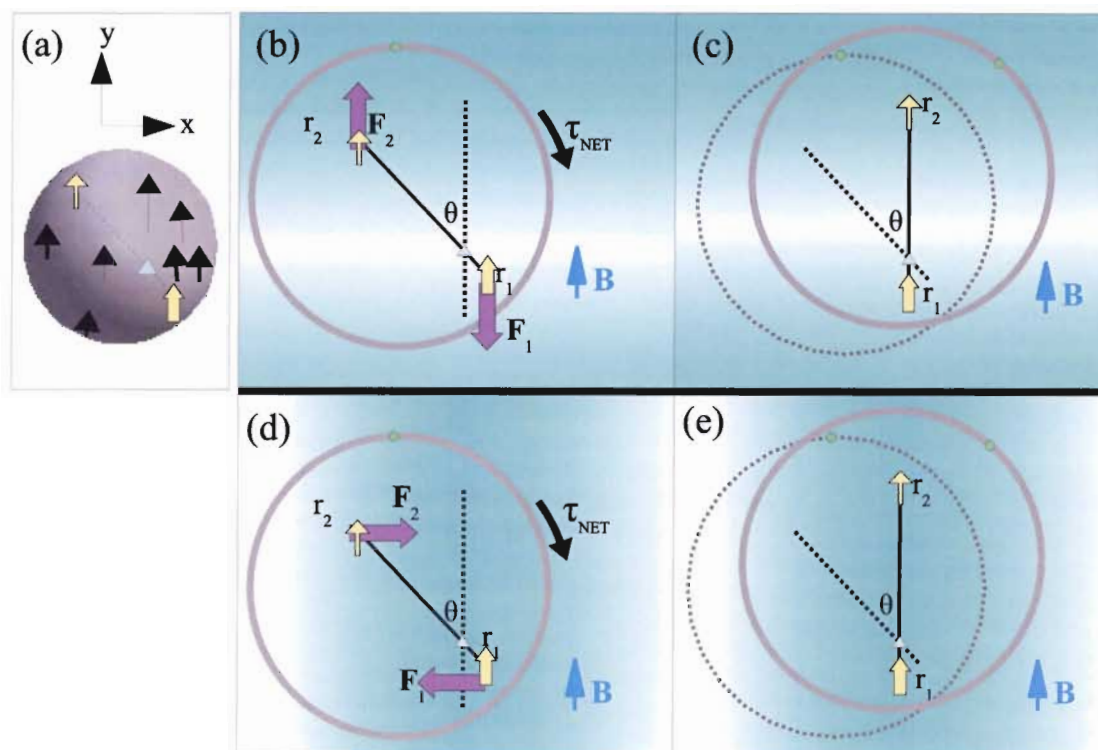
Figure 2.8: A torque acts on a bead in a magnetic field until it reaches a configuration where the total torque, $\tau_{net}$, equals zero. Thus, the bead has a preferred orientation and maintains alignment in a magnetic field. $\tau_{net}$ is caused by forces (purple block arrows) that arise from the gradients of the magnetic field in the x and y directions. We choose the gradients of $|\mathbf{B}|$ to be centred on the position of the net magnetic moment of the bead (triangle), $\mathbf{r}_{net}$. Cyan represents the strongest field. These gradients are representative of the field generated by a pair of magnets in the NSSN configuration. (a) Each ferrimagnetic particle within the bead (black arrow) contributes to $\mathbf{r}_{net}$, which lies directly above the tether point (Fig. 2.7). For illustration purposes, we decompose the net magnetic moment into two components located at $\mathbf{r}_1$ and $\mathbf{r}_2$ (yellow arrows). (b) For a gradient in $|\mathbf{B}|$ along the y direction, forces act on $\mathbf{r}_1$ and $\mathbf{r}_2$. These forces generate a torque until the vector between $\mathbf{r}_1$ and $\mathbf{r}_2$ is aligned with the field direction. (c) At equilibrium, there is no net torque. The equilibrium (solid line) and non-equilibrium (dotted line) bead orientations are shown, with a green dot representing a fixed position on the bead. (d) For the gradient in $|\mathbf{B}|$ along the x direction, the bead experiences a torque until the vector between $\mathbf{r}_1$ and $\mathbf{r}_2$ is parallel to the direction of the field. (e) At equilibrium, $\tau_{net} = 0$. The equilibrium and non-equilibrium bead orientations are shown.

For fields that are not centred at $\mathbf{r}_{net}$, the situation is not as easily described. In this situation, the bead's magnetic field environment is changed as a function of the rotation of the magnet. For this reason, $d\theta_{bead}/d\theta_{magnets}$ may not be constant throughout a full $360°$ rotation of the magnets. However, since there is no difference between the field generated by the magnet pair at $0°$ and $360°$, the bead will always have the same alignment after a full rotation of the magnets.

**From the point of view of energy**

It is a worthwhile exercise to analyze the system with energy arguments in order to gain additional intuition. The system includes the magnetic bead and the molecule to which it is tethered. The energy of the molecule depends on its extension, $\ell$, and can be calculated by integrating over the worm-like-chain model for semi-flexible polymers (see Section 4.4.1). The energy of the bead is determined by the magnetic field acting on it and hence its distance from the magnet pair, $\beta$. So, the total energy of the system can be summarized as

$$E_{total}(z_{mag}) = E_{DNA}(\ell) + E_{bead}(\beta) \qquad (2.1)$$

Since $z_{mag} = \ell + A + \beta$, the total energy of the system can be expressed as a function of $z_{mag}$ (Fig. 2.7c). So, the minimum energy of the system can be determined for a given $z_{mag}$. An understanding of how the bead interacts with the magnets and tether is required to accurately analyze the data collected from the magnetic tweezers. For the remainder of this thesis, we use $\beta$ to indicate the effective distance between the magnets and the bead, keeping in mind that the bead is never more than $5~\mu$m from the chamber bottom ($\beta \approx z_{mag}$).

## 2.3.4   Assembling the sample

Once the labeled DNA, antiDIG-coated beads, and streptavidin-coated sample chambers are available, assembling the sample is a simple process. Approximately $4~\mu$L of 5% w/v beads are incubated with $0.5~\mu$L DNA ($\sim$0.01 ng/$\mu$L) for 1.5 hours on a tumbler. This is then diluted into 3 mL of pulling buffer (150 mM NaCl, 10 mM Tris, 1mM EDTA, pH 8). This solution contains DNA molecules with one end bound to a bead and the other end free to bind to a streptavidin-coated surface. The solution can be stored at $4~°$C for many weeks.

To assemble tethers, the chamber is removed from any strong magnetic fields. The chamber is completely filled ($\sim$50 $\mu$L) with 0.05% w/v solution streptavidin-coated polystyrene (PS) beads (Spherotech, SVP-30-5, 3.18-$\mu$m diameter) and left to sit for about 10 minutes. These non-magnetic beads will bind to remaining biotin sites on the surface and, thus, are potential reference beads (see Fig. 4.6 for further details). Then $\sim$100 $\mu$L of the DNA-bead mixture is flowed through the chamber and incubated for 15 minutes to allow the DNA to bind to the surface of the sample chamber. It is also possible that the DNA binds to the non-magnetic streptavidin bead. If this situation arises, the diffraction patterns of the beads overlap and those beads would not be used in the analysis.

Place the chamber on the microscope stage and focus the objective lens on the bottom of the inside of the chamber. Focusing on this plane is straightforward if this surface is dotted with a permanent marker prior assembling the chamber. Bring the magnets close to the surface to draw any unbound beads to the top of the chamber. It is not necessary to wash the chamber of freely floating beads unless they obstruct the image. Most of the remaining beads are either superparamagnetic, tethered by DNA to the surface and exhibiting Brownian motion, or non-magnetic, streptavidin-coated PS beads bound directly to the surface. A small number of the remaining beads are immobilized on the surface nonspecifically. Note that finding a tethered bead is made easier if the PS and superparamagnetic beads are different sizes. The sample is now ready for experiments.

# Chapter 3

# Determining the z position of the bead

We wish to extract the DNA extension (end-to-end distance) from the magnetic tweezers apparatus. Since video microscopy cannot directly visualize the DNA, we use the z position (height) of the bead to infer the extension of the DNA molecule perpendicular to the surface. The height is determined from the diffraction ring pattern generated by an out-of-focus bead.

## 3.1   Diffraction Ring Pattern

The diffraction ring pattern is composed of concentric, alternating rings of light and dark and is the result of interference of light as it refracts at the bead-solution interface (Fig. 3.1). As the separation between the bead and the objective lens decreases, the diffraction pattern from bright light illumination tends to get larger and more diffuse. We put a filter between the light source and the sample to transmit only red light, thus minimizing the range of wavelengths which generate our diffraction pattern and enhancing the contrast between the light and dark rings. Any colour filter can be used, however, it was empirically determined that the red filter passes the highest intensity in our apparatus.

Since algorithms involving 2D analysis are often computationally expensive, we simplify the 2D diffraction ring pattern by locating the centre of the pattern and calculating a radial intensity profile from that centre. We then use this profile to determine the height of the bead.
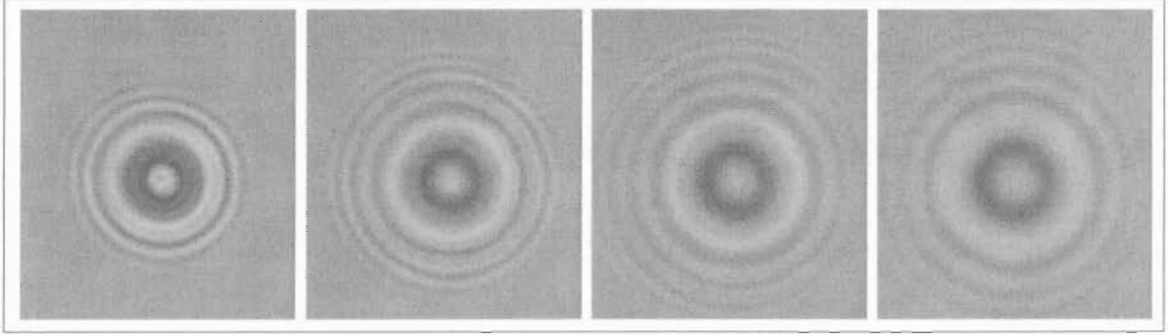
Figure 3.1: The diffraction pattern of a single bead expands as the bead-to-objective lens distance decreases. These images of a bead stuck to the cover glass surface are taken at objective lens height increments of 2 $\mu$m.

### 3.1.1 Centre-finding subroutine

For a large range of heights, the centre of the diffraction pattern is a local intensity maximum. The centre of the diffraction pattern can be determined to sub-pixel resolution for 100x magnification. Our centre-finding subroutine calculates the intensity centroid, $(x_0, y_0)$, of a $2N + 1$ by $2N + 1$ square region.

$$x_0 = \frac{1}{2N+1} \sum_{j=-N}^{N} \frac{\sum_{k=-N}^{N} x_{j,k}(I_{j,k})^{24}}{\sum_{k=-N}^{N} (I_{j,k})^{24}} \tag{3.1}$$

Equation 3.1 shows the mathematical form of the centroid calculation for $x_0$, which has then been averaged over $2N + 1$ rows. Here $x_{j,k}$ represents the position of a pixel with indices $(j,k)$ and $I_{j,k}$ its intensity. The intensity is raised to a high power (24) to amplify the central peak, as it is plateau-like. If the image is noisy, the centroid calculation could be biased. For our images, however, we obtain similar resolution and values from our diffraction pattern centre measurements from both the centroid method implemented in this thesis and a separately developed 2D cross correlation method.

The centroid algorithm is most efficient if the $2N + 1$ by $2N + 1$ square is completely within the zeroth-order bright spot. This is accomplished if $N$ is less than the position of the first minimum of the radial intensity pattern, which can be calculated automatically for each frame if the 'auto +/-' option is selected. Otherwise, the user may specify a constant value for $N$.

The centre-finding subroutine requires an initial guess or input of the coordinates of the centre to within a few pixels. This input is initially specified by the user double-clicking on the screen near the centre of the pattern. The first $(x_0, y_0)$ serves as the input in subsequent iterations. This algorithm is usually iterated two or three times for a single frame until the calculated value of $(x_0, y_0)$ is equal to the previous iteration. This value is passed on to the next frame as input. The iterative process is necessary because the initial input for a frame may be several pixels away from the actual centre.

### 3.1.2 Radial intensity profile

Once the centre position, $(x_0, y_0)$, has been calculated using the centroid method, a radial intensity profile of the diffraction pattern can be constructed. Let $(x0, y0)$ be the integer portion of the centroid values $(x0 = \lfloor x_0 \rfloor \ y0 = \lfloor y_0 \rfloor)$. We use the intensity values of the quadrant from pixels $(x0 - 1, y0 - 1)$ to $(x0 + 99, y0 + 99)$. In other words, our algorithm averages over the lower right-hand quadrant of the pattern, plus the two adjacent rows and columns to obtain a more accurate intensity for the $r = 0$ pixel bin. The full image can be used, but is computationally expensive. The radial distance, $r$, for each pixel in the quadrant, denoted by position $(i, j)$, is given by $[(x_i - x_0)^2 + (y_j - y_0)^2]^{1/2}$; where $x_i$ and $y_j$ represent the midpoint of each pixel. The intensity from each pixel contributes to the profile in the bin $\lfloor r \rfloor$. Thus, if the midpoints of two pixels are 3.7 and 4.2 px from the centroid position, then the intensity values will contribute to bins 3 and 4, respectively. Once binned, the sum of the intensity values in each bin should be divided by the number of contributions to yield the average radial intensity profile, in units of pixels from the $(x_0, y_0)$ centroid position. Fig. 3.2 presents an example of a radial intensity profile.

## 3.2 Calibration

The z position, or height, of the bead is determined through a two-step process. The first step, *Calibration*, compiles information from images recorded at known heights. *Measurement*, the second step, uses the calibration data to analyze images in real time to extract the z position of the bead.

To determine the z position from images of the xy plane requires a calibration set which
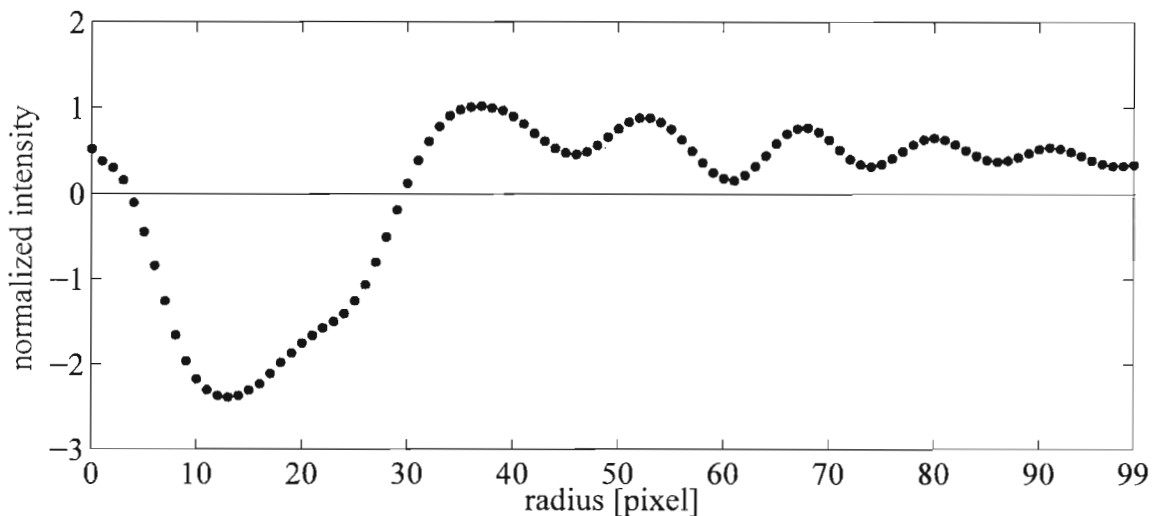
Figure 3.2: Radial intensity profile of a single bead where $r = 0$ corresponds to the sub-pixel centre of the diffraction pattern. The intensity values are averaged over a quadrant of the image. The raw radial intensity profile is then normalized such that the mean intensity is 0, and its standard deviation is 1.

correlates information from the images with known heights of the bead. The choice of information affects the resolution and range of the extracted height information. We begin to calibrate our system by stepping the objective lens by known distances and averaging the radial intensity profile of a fixed bead over many images for each step (Fig. 3.3). We have tried the calibration by taking three different types of information from the radial intensity profile: position of the first minimum, mean phase and the correlation of the full radial profile.

The following sections compare the usefulness of the three approaches by considering the range of allowable measurements and resolution of each. A measurement range of at least 6 $\mu$m is required, even though this is much larger than any expected change in height of the bead for the molecules we plan to study. Unfortunately, the effects of instrument drift in x,y and z, often result in measurements spanning the entire 6 $\mu$m range.
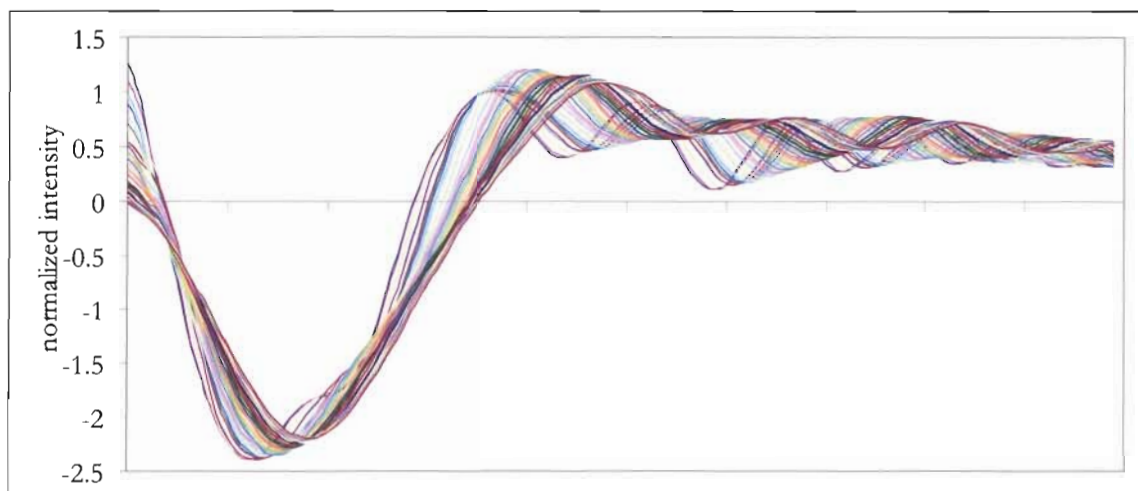
Figure 3.3: The set of radial intensity profiles for a fixed bead obtained over forty consecutive 0.2 $\mu$m steps of the objective lens. The position of the first minimum increases as the objective lens moves towards the chamber or, equivalently, the bead-objective separation decreases.

## 3.2.1   Position of first minimum

Analytical solutions for the diffraction pattern generated by an opaque sphere have been modeled by Sommargren and Weaver [41, 42]. Although our attempts to model our observed pattern using these formulations ignored the more complex optical path in our instrument, including the lenses and incoherent light source, some general relations were realized. We predicted that as the bead height increases (which is equivalent to the objective lens moving away from a bead stuck to a cover glass), the position of the first minimum in the radial intensity profile (min pos) should decrease. This is a linear relationship and provides a link from the real-time radial intensity profiles to height information. We have found that the prediction is true over at least a 6 $\mu$m range. Fig. 3.4 illustrates the linear relationship for objective lens steps of 0.2 $\mu$m over twenty-four steps. If the expected change in height of the tethered molecule is of order 1 $\mu$m, the corresponding change in min pos is 1 pixel (75 nm). At the time this algorithm was implemented, the min pos shift was comparable to the noise of the measurement because the measurements were not corrected for drift. Without drift correction, the min pos method of z analysis has a resolution of $\sim$1

$\mu$m in height determination which is insufficient for our experiments. With drift correction, the resolution improves.
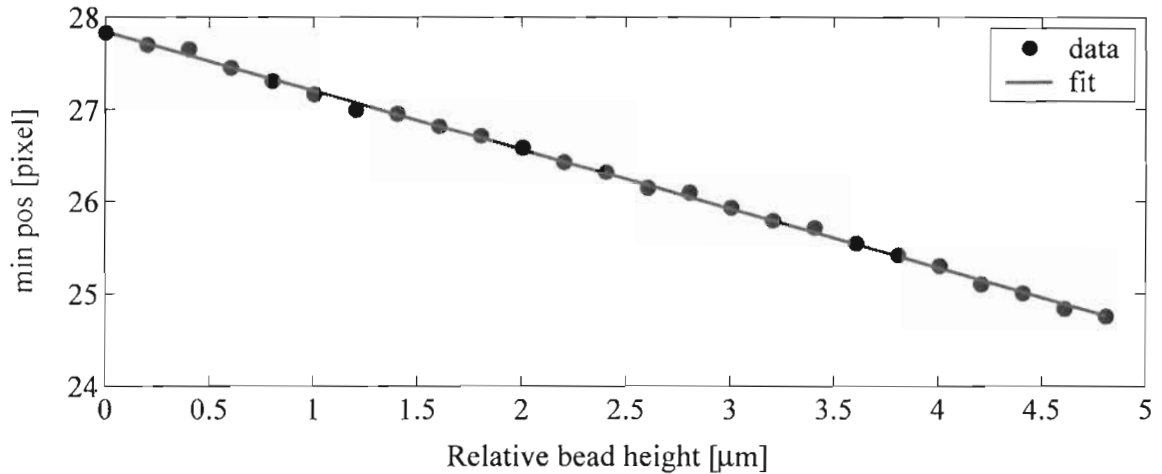


Figure 3.4: A linear relationship exists between bead height and position of the first minimum of the radial intensity profile (min pos). The min pos of a bead is determined for twenty-four consecutive 0.2-$\mu$m increments of the objective lens. Since the bead is stuck to the surface of a cover glass, the objective lens height is equivalent to the relative height of the bead. The min pos decreases as the height of the bead increases.

## 3.2.2  Average phase

Another calibration method is to calculate the average phase of the radial intensity profile for known heights and fit this relationship to a polynomial (Fig. 3.5). The mean phase is obtained by taking a Hilbert transform of a portion of the radial intensity profile and calculating the average of the returned phase values [2]. A Hilbert transform is a mathematical algorithm which extracts the phase of a data set from the imaginary component of the Fourier transform. In our implementation of this technique, the Hilbert transform is taken over the 100-pixel radial intensity profile and we select the most favourable region over which to take the average. We find that the average phase technique is sufficient for low resolution measurements with $\sim$100 nm resolution in z under the best conditions. However, this method is prone to errors since the range over which the average phase is

determined depends on the bead height and is not consistent when a bead is moved by 6 $\mu$m.

(a) Hilbert transform

(b) mean phase versus height
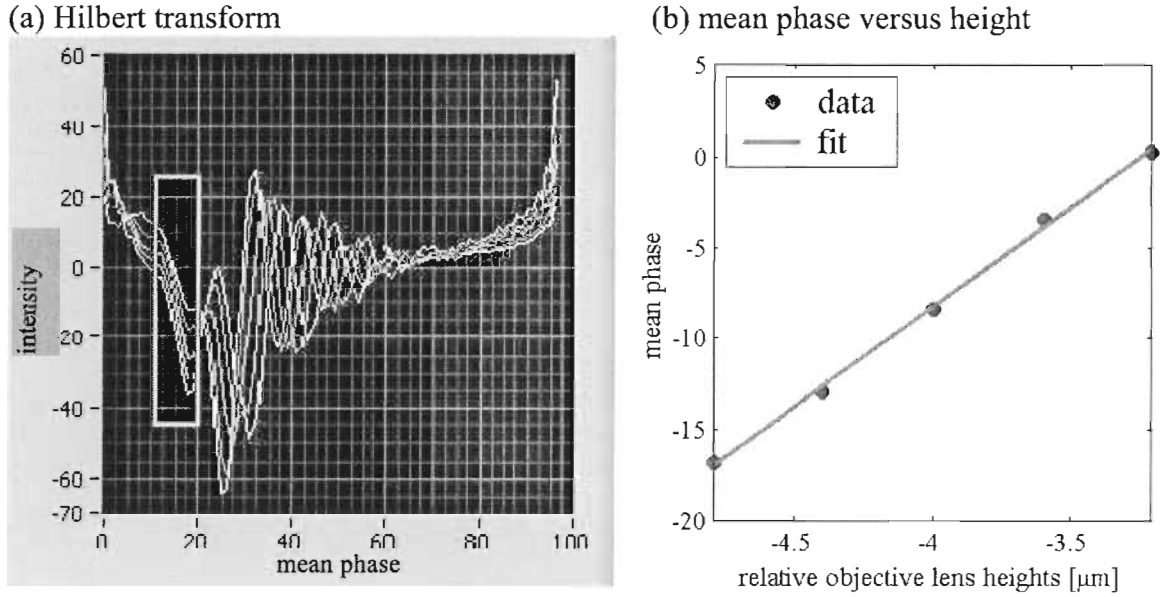


Figure 3.5: (a) The Hilbert transform of five radial intensity profiles are shown in different colours. The box indicates the region over which the average phase is calculated. (b) For this particular region of the set of Hilbert transforms, the relationship between average phase and height is nearly linear. When fit to a function, it can be used to extract height information of images in real time.

### 3.2.3   Correlation of full radial intensity profile

In this final technique, the correlation between the calibration set and our real-time radial intensity profile is used to calculate the z position of our bead. In this case, the calibration set consists of just the averaged radial intensity profiles $I_i(r)$ and the corresponding height information. The correlation between the real-time image and each calibration image $i$ is calculated by

$$s_i = \sum_{j=0}^{99} a_j b_{i,j} \tag{3.2}$$

where $s_i$ is its correlation with $I_i(r)$, $a_j$ denotes the intensity of the $j^{th}$ pixel of the real-time radial intensity curve, and $b_{i,j}$ is the intensity of the $j^{th}$ pixel of the $i^{th}$ calibration curve.

The correlation plot of $s_i$ versus the corresponding heights for the $i^{th}$ calibration curve shows a clear maximum (Fig. 3.6). Nine points, consisting of the four points on either side of the maximum value, are fit to a fourth-order polynomial. The position corresponding to the maximum value of this function gives the calculated z position of the real-time curve. A perfect match between the $i^{th}$ calibration curve and the real-time curve gives a correlation value of $N$, where $N$ is the number of points in the radial intensity profile which have been normalized to have a standard deviation of 1.
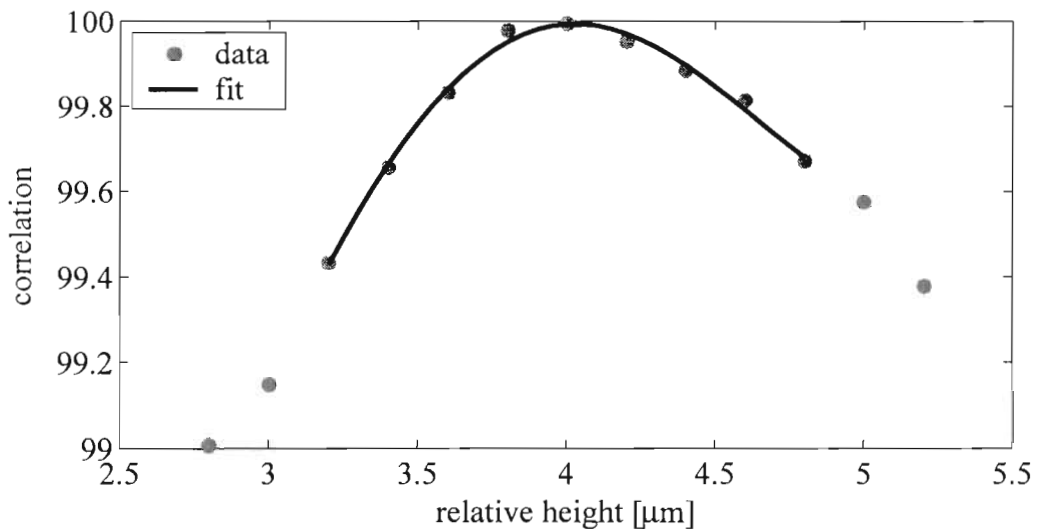


Figure 3.6: The correlation plot is calculated from the correlation of the calibration set with the sample radial intensity profile. Nine points are fit to a fourth-order polynomial, and the maximum of this function gives the relative height of the bead.

The correlation of the radial intensity calibration technique is sensitive to minor changes in the pattern caused by changes in the bead height because the whole radial intensity profile is taken into account. A typical calibration set is taken over forty 0.2-$\mu$m steps, yielding a useful measurement range of about 6 $\mu$m since at least four points are required on either side of the correlation maximum. Currently, the resolution of each x and y measurement attained using this method is approximately 6 nm, while the z measurement resolution is approximately 75 nm (Fig. 3.7). See Section 5.1 for ways to improve the resolution.
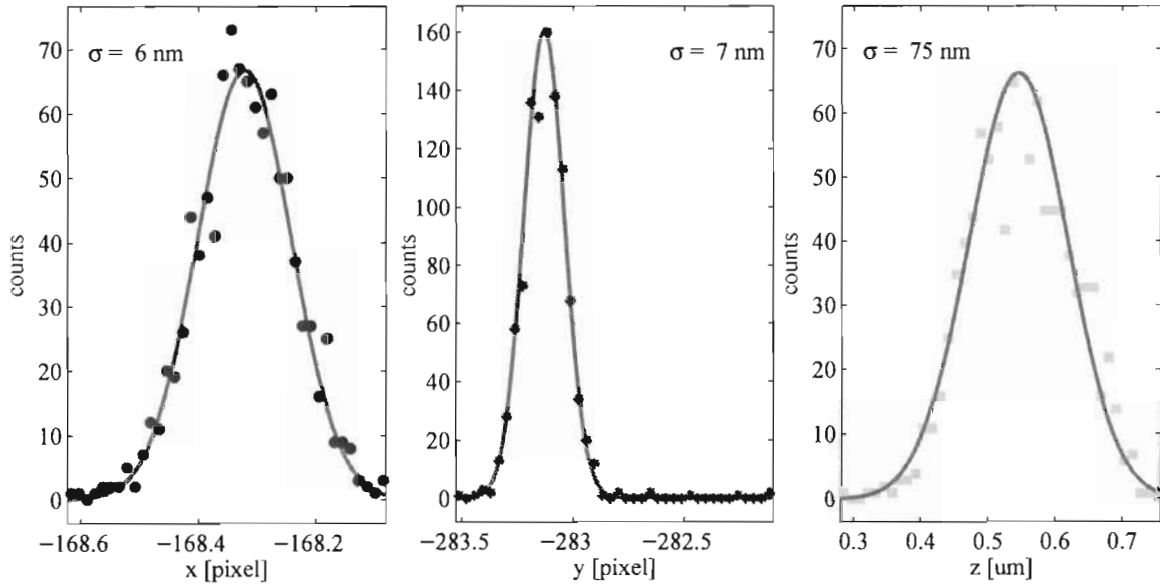
Figure 3.7: The drift-corrected (x,y,z) position of a bead stuck to the glass surface is measured for 1000 frames. The histogram of the positions (points) are fit by a Gaussian distribution (solid line) to yield the resolution of the measurement (standard deviation, $\sigma$). Each pixel is approximately 75 nm.

In summary, we have developed three different techniques to determine the height of the bead based on the radial intensity profile of its diffraction pattern. Each method is limited in the range and resolution of heights it can determine. The correlation of the radial intensity profile technique is selected to determine the bead height in our instrument because it has the highest resolution over the desired 6 $\mu$m range.

## 3.3  Measurement

Ideally, once the calibration step has been completed, a measurement of the z position of the bead can be made. In conjunction with the data from the centre-finding subroutine, the (x,y,z) coordinates can be determined in real time at 15 Hz. However, in practice our measurements are influenced by instrumental drift.

### 3.3.1 Drift

Drift measurements were conducted by evaluating the position of a bead stuck to a glass slide every two minutes for several hours. The instrument is located in a temperature controlled area, with an external air conditioning unit that regulates the temperature to within $\pm 0.5\,°C$.

The drift measurements revealed two different situations. The first is *regular* drift which may be due in part to the gradual settling of the objective lens. The magnitude of this drift is approximately 0.7 $\mu m$/hour in x, 0.5 $\mu m$/hour in y, and 1 $\mu m$/hour in z.

The second type of drift, which is not always present, takes the form of an oscillation in the x, y and z directions (Fig. 3.8). It has a period of about 25 minutes, and appears correlated in all three directions. There is no correlation between the oscillating drift and air currents, slip in the motorized controller for the fine focus knob, the floating optical table, or vibrations from nearby computer units. A correlation with temperature is suspected but has not been verified. The oscillatory drift is also subject to *regular* drift. The amplitude of the oscillation is about 0.3 $\mu m$ in x, 0.4 $\mu m$ in y, and 1.2 $\mu m$ in z.

Despite the two varieties of drift that plague the measurements made using our magnetic tweezers, it is still possible to extract information that is free of drift. This is accomplished with the help of a reference bead in the same field of view as the measurement bead. A reference bead is stuck to the inside surface of the chamber and provides a direct measurement of both forms of instrumental drift. For experimental measurements, the trajectory of the reference bead is attenuated with a low-pass filter and then subtracted from the measurement bead coordinates. These new bead measurement coordinates are thus corrected for instrumental drift. See Fig. 4.6 for more details.

### 3.3.2 Spherical aberration

In addition to instrument drift, there exists a systematic error in the measured heights. The apparatus uses an oil-immersion objective lens to image the bead within the sample chamber. This lens is used to capture as much information as possible from the diffraction ring pattern. The use of an oil-immersion lens is subject to spherical aberration which is the result of the mismatch of index of refraction, $n$, between the immersion oil (and cover glass which are both $n_o = 1.515$) and the water within the chamber ($n_w = 1.333$). If the magnetic
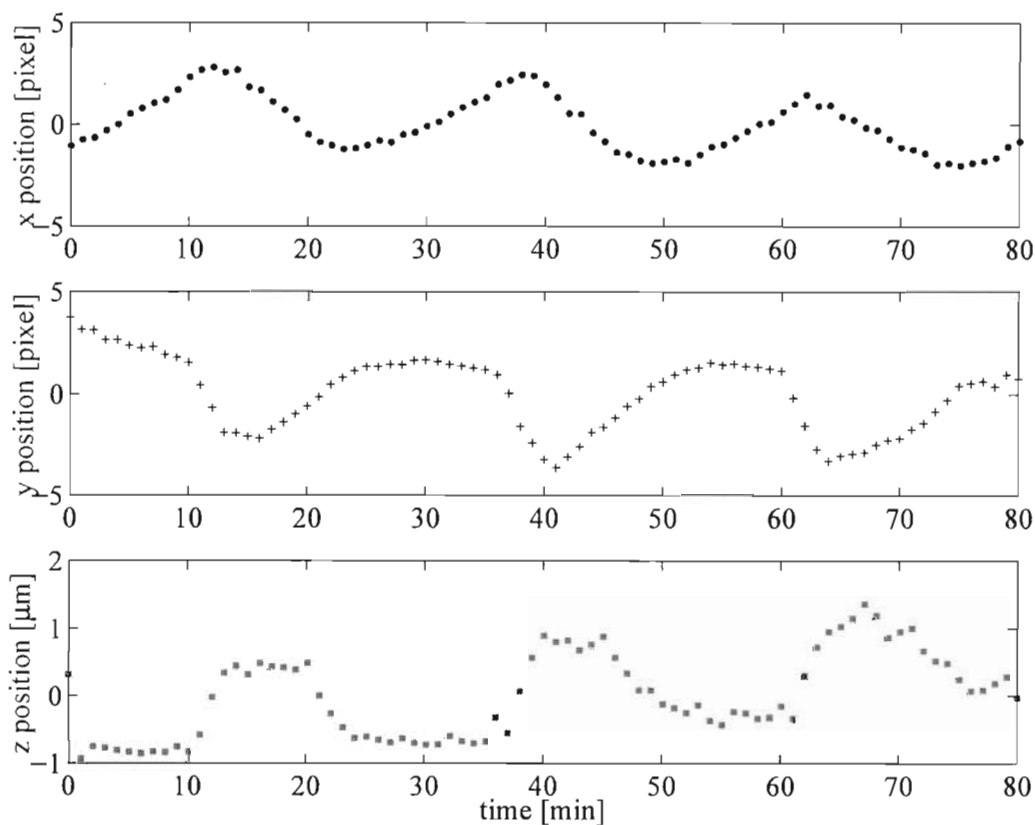
Figure 3.8: The (x,y,z) position of a stuck bead was measured for 80 minutes. Oscillations were detected in all three axes with a period of $\sim$25 minutes. Each pixel is equivalent to approximately 75 nm.

tweezers were outfit with a water-immersion objective lens, spherical aberration would not be present because there would be water on both sides of the interface.

Spherical aberration results in an apparent height of an image different from the real height, because of refraction of the light beam at an interface (Fig. 3.9). When the oil-immersion objective lens is focused directly above the water-oil interface, spherical aberration is negligible. The effects of spherical aberration become more prominent as the focal plane moves further into the aqueous sample chamber. That is, as the extension of the molecule increases, the correction for spherical aberration becomes more necessary. A tethered bead under upward force is located several microns above the surface of the cover glass, and its image is therefore affected by this problem. In this thesis, we apply the

maximum correction for spherical aberration.

During calibration, the objective is stepped known distances in oil while the bead remains fixed in space (Fig. 3.10). The change in distance between the bead and the objective lens, $\Delta D$, is real and completely in oil; $\Delta D = \Delta d_o$. During measurement mode, it is instead the bead which changes its height in water while the objective lens stays fixed. So the difference in apparent height of the bead is wholly due to a change in the distance the light travels through water. That is, $\Delta D' = \Delta d_w$, where the primed variable indicates an apparent height. The observed change in $d_w$ must be corrected for spherical aberration.

If the calibration images are used to determine the change of height of the bead in water, the difference in apparent height from the measurements must be multiplied by a correction factor. For this system, the correction factor is calculated to be $n_w/n_o = 1.333/1.515 = 0.88$. Note that measured heights are relative, not absolute, because there is no reliable reference height for our system. So, it is the difference between these values which is meaningful (Equation 3.3).

$$
\begin{aligned}
D \tan \theta_w &= D' \tan \theta_o \text{ for small } \theta \\
D &\approx D' \frac{n_w}{n_o} \\
\Delta D &\approx \Delta D' \frac{n_w}{n_o}
\end{aligned}
\tag{3.3}
$$

In summary, determining the z position of the bead involves a calibration step, in which the radial intensity profile is recorded for known heights of the bead, and a measurement step, where the real-time profile is correlated against the calibration set to output the height of the bead. A reference bead is required to quantify the instrumental drift in the z direction. The drift can then be subtracted from the motion of the tethered bead. Also, because we are using an oil-immersion objective and there is a water-oil interface, a correction for spherical aberration must be made to the apparent height of the bead. The height of the bead is required to determine the extension of the tethered DNA molecule, $\ell$.
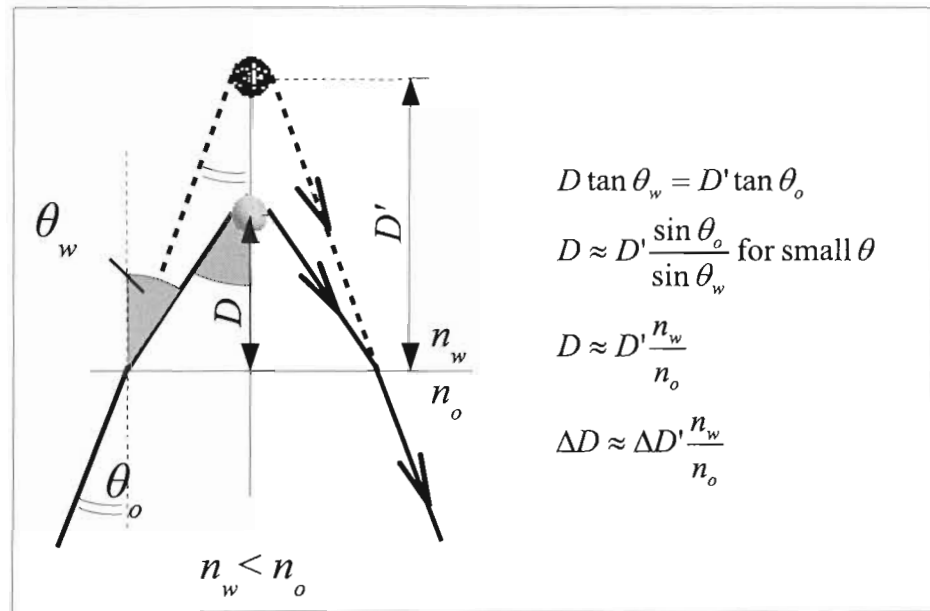
Figure 3.9: Spherical aberration causes the bead to appear at a height, $D'$, which is different than the actual height, $D$. This ray diagram illustrates the origin of the bead's apparent position due to the refraction of light as it passes through the water-oil interface. $n_w$ and $n_o$ are the index of refraction of water and oil, respectively. During the measurement mode when the bead changes its position in water, calculated height values are based on the calibration which involved known steps through oil. A correction factor of the ratio between $n_w$ and $n_o$ must be multiplied by the apparent measured heights to obtain the actual heights. All bead heights are relative values.
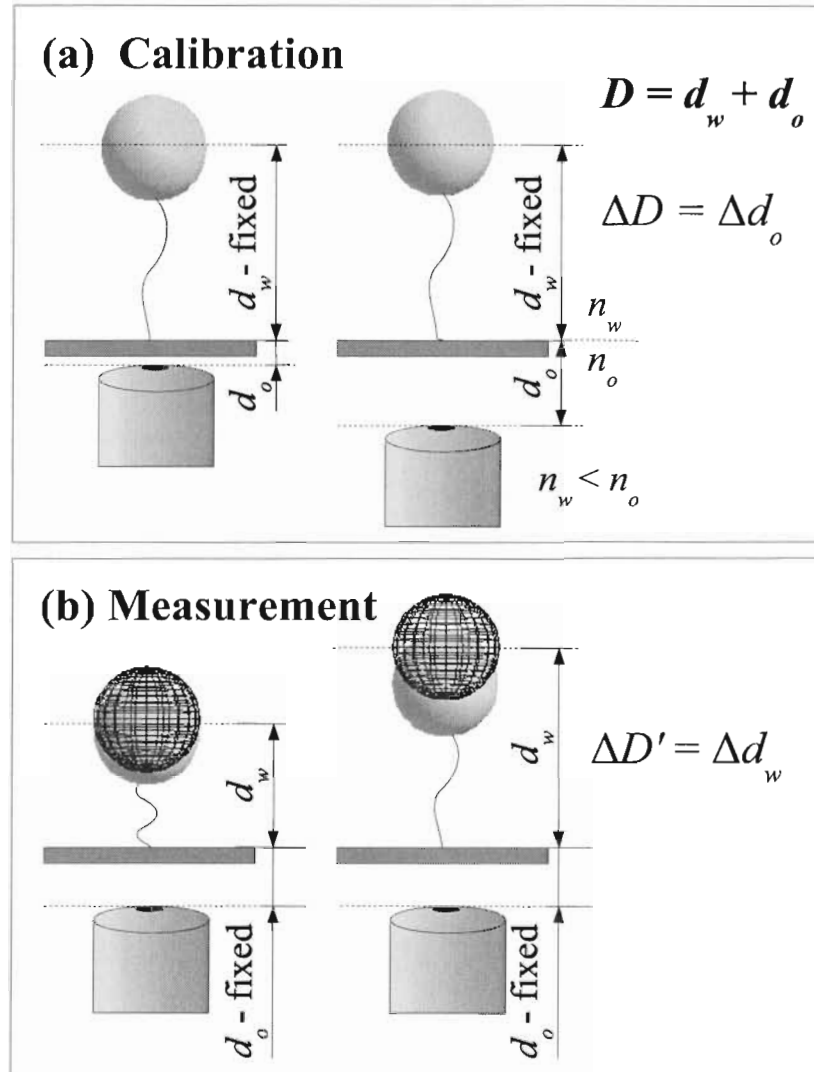
Figure 3.10: The discrepancy between the Calibration and Measurement modes arises from the difference in refractive index between the immersion oil/glass and the water in the sample chamber. The origin of the changing diffraction pattern used in the analysis is the change in the distance between the bead and the objective lens, $D$. The effective distance is separated into the portion in which light travels through water, $d_w$, and the portion in which light travels through oil, $d_o$. (a) During Calibration, the relative heights are real. (b) During the Measurement mode, the measured height, $D'$, is subject to bias caused by spherical aberration and is based on an apparent image (outlined sphere). Therefore, the change of height in the Measurement mode is also apparent, $\Delta D'$ and requires a correction factor.

# Chapter 4

# Force characterisation of the magnetic tweezers

In this chapter, we characterise the force acting on a superparamagnetic bead in the magnetic tweezers apparatus using both calculations and experimental data. Macroscopic changes in the magnet height are required to appreciably change the pulling forces generated in the magnetic tweezers. In general, the force acting on the bead, $\mathbf{F}$, is given by the gradient of the inner product between the magnetic moment of the bead, $\mathbf{m}$, and the external magnetic field of the magnets, $\mathbf{B}$ [43]:

$$\mathbf{F} = \nabla(\mathbf{m} \cdot \mathbf{B}) \tag{4.1}$$

We have calculated the magnetic fields from Gauss' law for magnetism and measured them using a Hall probe. The magnetic moment of a bead can be calculated as a function of the magnetic field, based on the manufacturer's magnetisation curve and density data for a bulk sample of beads. Therefore, we can calculate the expected pulling force on an *average* bead. These predictions are tested by directly measuring the force via Brownian motion of a tethered bead. See Figure 4.1 for the coordinate frame that will be referred to in the remainder of this chapter.

Ultimately, the practical interest of this analysis is to obtain a reliable relationship between the force exerted on the bead and the magnets-to-bead distance, $\beta$. For example, future users of the magnetic tweezers will be able to optimize the magnet set-up to provide

the most linear force-distance dependence in the range of required forces for a particular experiment. Appendix C discusses ways to increase the maximum pulling force with small changes to the existing equipment.
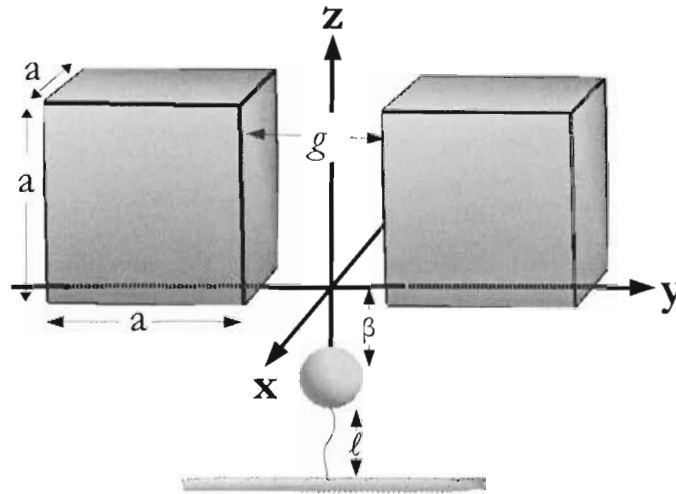


Figure 4.1: The coordinate system for magnet pair with respect to bead position. The short axis of the magnet pair lies along the x axis, while the long axis is along the y axis. Only $z < 0$ is accessible to the bead. $\beta$ is defined as the distance between the magnet pair and the bead, and is the experimental parameter we control by moving the magnets away from the sample chamber, which stays fixed. In the calculations, however, we keep the magnets fixed and move the bead along the z axis. $\ell$ refers to the extension (end-to-end distance) of the tethered DNA molecule. Measurable force differences are achieved only if $\beta$ is changed by distances of order millimeters. $a$ refers to the dimensions of the rare-earth magnets ($a = 0.5"$ for our cube magnets), and $g$ is the gap between the magnet pair and is one the order of millimeters. This figure is not drawn to scale.

## 4.1   Calculating fields and forces

Understanding the magnetic field environment surrounding the bead is the first step in determining the forces acting on the bead. In this section, we model the external magnetic field and calculate the magnetic moment of an average bead.

### 4.1.1 Calculating B-fields

The magnetic fields, **B**, arising from the relatively simple geometry of two cubic permanent magnets with side length $a$, separated by gap distance $g$, can be calculated. There are two main magnet configurations which are relevant to the magnetic tweezers instrument (Fig. 4.2). In both cases, the magnets are separated by a magnet holder machined from a non-magnetic material, phenolic. The NSSN configuration describes the situation in which the magnetisations are anti-parallel, and are perpendicular to the long axis. The NSNS configuration refers to when the magnetisations of the magnets are parallel to one another, and to the long axis of the magnet pair.
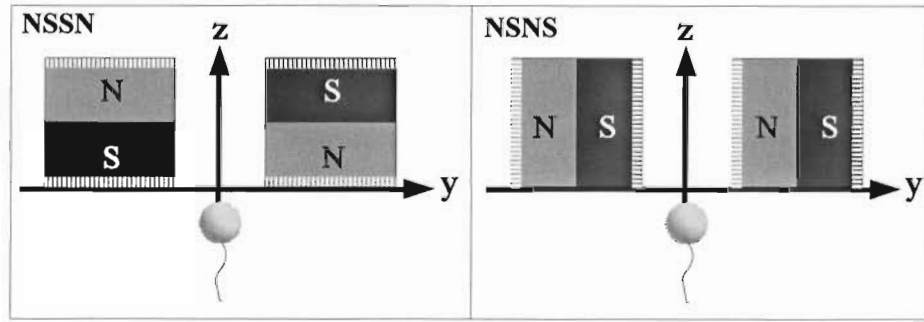


Figure 4.2: A view of the magnet pair along the yz plane showing the two relevant magnet configurations. The dashed lines on both diagrams show the sides involved in the magnetic scalar potential, $\psi$, calculation. These figures are not drawn to scale. (a) The NSSN configuration involves two magnets, which are oriented parallel and anti-parallel to the zaxis, separated by a spacer. This configuration provides the most useful field gradient for pulling experiments. (b) In the NSNS configuration, the magnetisation direction of both magnets is parallel to the y axis.

The magnetic field at the location of the bead can be calculated from the magnetic scalar potential, $\psi$:

$$\mathbf{B} = -\nabla\psi \tag{4.2}$$

Contributions to the magnetic scalar potential are made only from the surfaces that are perpendicular to the direction of the magnetic field. For our simple magnet geometry, we need to sum over $\psi_i$ of four surfaces (labeled by dashed lines in Figure 4.2) to obtain the full $\psi$. The contribution from each surface can be calculated as follows:

$$\psi_i = \int_{S_i} dS \frac{M1}{\sqrt{(x-x_0)^2 + (y-y_0)^2 + (z-z_0)^2}} \tag{4.3}$$

where $(x_0, y_0, z_0)$ represents the observation point (bead), $S_i(x, y, z)$ is the $i^{th}$ surface of the magnet, and M1 is the magnetic moment of the magnet.

**B** has been calculated analytically from $\psi$ using Equation 4.2 and then evaluated for specific positions using a program written in the mathematical software package Maple 9.5. If the bead is located along the z axis, $B_y$ is the only component of the field. Figure 4.3 shows $B_y$ along the z axis of the field from the magnet pair for different gap sizes in both the NSNS and NSSN configurations.

## 4.1.2 Measuring B-fields

To verify that our calculations were accurate and physically correct, we used a Hall probe (Group 3, DTM-151 and MPT-237-75) to measure the magnetic field of our magnet pair as a function of the distance along the z axis. The Hall probe was held stationary and parallel to the microscope stage, while the magnets were moved along the z axis via the PI linear positioner. The Hall probe outputs a voltage which was calibrated to give the magnetic field in units of Gauss. The linear calibration factor was obtained by comparing the voltage to the digital readout on the Hall probe controller over a large range of magnetic fields. During an experiment, the field is not accessible to the bead for $\beta < 0$. However, we chose to confirm the accuracy of our field calculations by employing a special magnet holder that allows the Hall probe to scan directly through the centre of the magnets while keeping the magnets a constant distance apart. We measured the $B_y$ component of both the NSNS and NSSN magnet configurations at a number of different gap sizes (only one is presented here). The measured results (circles) are superimposed on the calculated quantities (smooth line) with the same gap size. Figure 4.3 shows very good agreement between the measured and calculated field values in both the NSNS and NSSN configurations.

The M1 value was selected such that the calculation fit the data (M1 $\approx$ 3000 G), but then remained constant for each subsequent calculation. According to the manufacturer, the maximum remnant magnetic moment of our cube magnet is 13,200 G (K&J Magnetics Inc., USA).
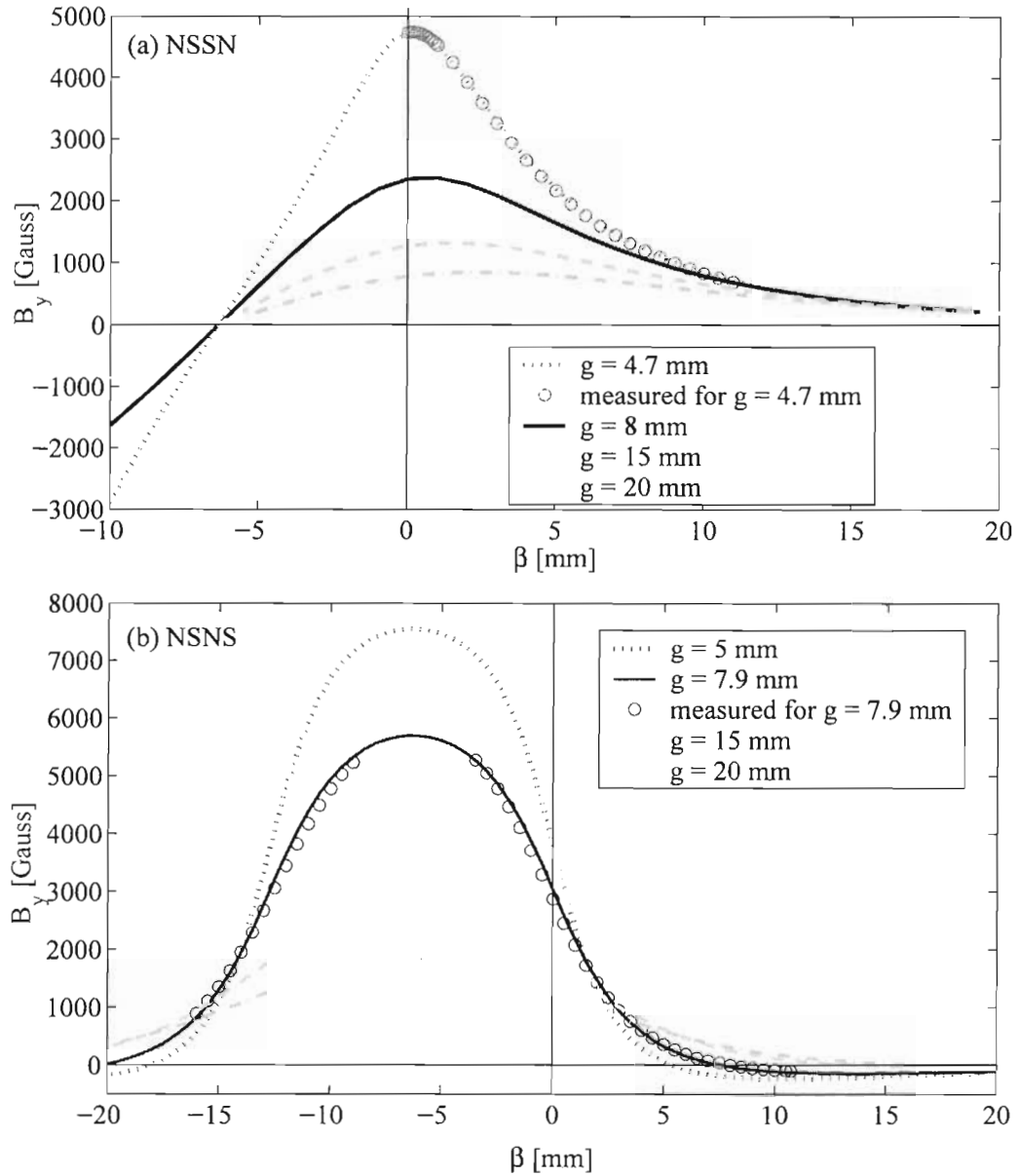
Figure 4.3: The magnetic fields along the z axis from NSSN and NSNS configurations have been calculated for different gap sizes, measured for a particular gap size and show correlation. The magnet-to-bead distance, $\beta$, equals zero when the bead is located on the bottom plane of the magnet pair. Note that only $\beta > 0$ is accessible to the sample. (a) The NSSN field mainly decreases monotonically in the accessible region. (b) The NSNS field has a minimum in the accessible region.

### 4.1.3 Calculating forces

We calculate the pulling force from the numerical solutions of the experimentally confirmed magnetic fields generated by the magnet pair. As described in this section, we apply Equation 4.1 to evaluate the x, y and z components of the force for any point. For simplicity and geometric symmetry, we present only the forces along the z axis (x=y=0).

Besides the field, the other relevant quantity required to determine the force is the magnetic moment of the superparamagnetic bead, **m**. It depends on the external field strength as seen in Figure 2.6, and can become saturated. The magnetic field strengths in this apparatus span both the saturated and unsaturated regions of the induced magnetic moment curve, so we treat **m** as a function of **B**. This has not always been done in analysis of this type of experiment [3, 8, 44].

Figure 4.4 shows the calculated forces as a function of magnet-to-bead distance, $\beta$, for the NSNS and NSSN magnet configurations. In both configurations, the bead actually feels a pushing force in some range, which is contrary to the expectation in [6]. In some cases, the bead is pushed towards the substrate instead of being pulled away from it. The switch between pulling and pushing forces occurs at the critical point of the **m·B** versus $\beta$ curve (Fig. 4.4). **B** mostly determines the shape of the **m·B** curve, but since the relationship between **m** and **B** is nonlinear at field strengths near saturation, it is more appropriate to consider the **m·B** curve.

In the NSNS configuration, the pushing region is sandwiched between two pulling regions which provides unnecessary experimental difficulty. A smaller gap spacing between magnets corresponds to a larger pushing force but a shorter magnet height range over which these pushing forces are felt. Larger gap sizes, say $g = 15$ mm, can provide a pushing force on the order of 0.01 pN over a range of 7 mm.

From the calculations, the NSSN configuration can also generate small pushing forces but these occur near $\beta = 0$. Pushing forces are not accessible when $g = 5$ mm, and end by $\beta = 1.25$ mm when $g = 15$ mm. We choose only to perform experimental studies with the NSSN magnet configuration with $g = 5$ mm because we prefer only pulling forces to act on our bead and because we have access to a range of appropriate forces. In our current set-up, we are unable to experimentally determine the magnitude of the pushing force as the bead would be pushed into the substrate which obstructs its motion. However, a sample
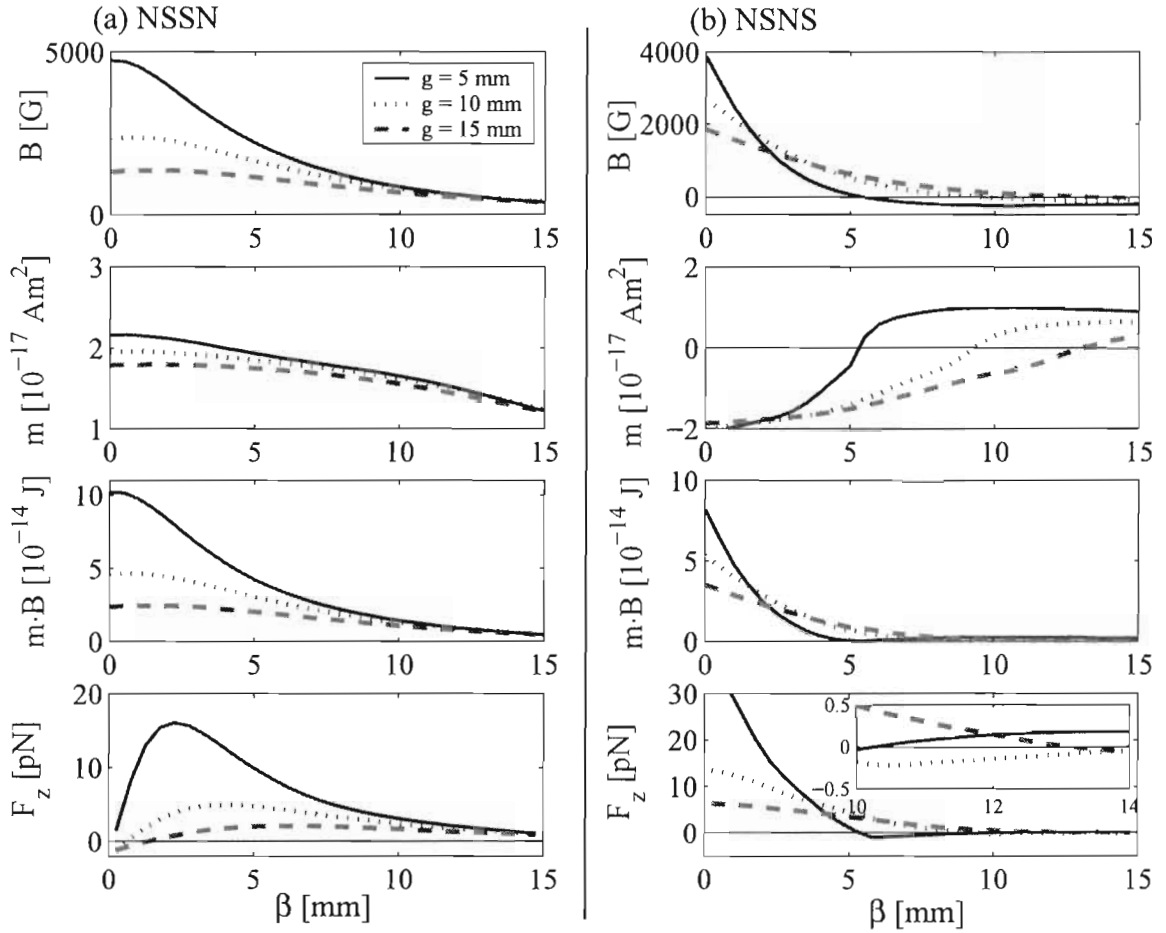
Figure 4.4: This series of graphs provides a visualization of steps involved in the force calculation as a function of the magnet-to-bead distance, $\beta$ for (a) NSSN and (b) NSNS configurations. Calculation for different gap sizes, g, are presented. The magnetic field, **B**, (top) is calculated from Equation 4.2. The magnetic moment of the bead, **m**, (middle top) is calculated for an average 2.8-$\mu$m-diameter bead based on the manufacturer's data and is a function of **B**. **m·B** (middle bottom) is always positive, since the magnetisation of the bead is always parallel to the direction of the field. The pulling force, $F_z$, (bottom) is given by the gradient of **m·B**. At points along the z axis, this force is in the z direction. Notice that the field generated by the magnet pair spans both the saturated and unsaturated regime of the magnetic moment of the bead.

could be constructed with the molecule tethered at the top of the chamber. This situation would allow us to quantify the force acting in the negative z direction by *pushing* the bead and stretching a single molecule.

The magnetic tweezers instrument is capable of reliably exerting sub-pN forces on a tethered bead. By comparing our force calculations for different magnet pair separations, we notice that gap size does not significantly affect the range of low forces accessible for large $\beta$ (Fig. 4.4).

## 4.2   From Brownian motion (noise) to data

Employing the relation first used by Strick *et al.* in 1996 [17], we can extract the pulling force from measurements of the bead position as it undergoes Brownian fluctuations in an aqueous environment, and the measured extension (end-to-end distance) of the DNA. Experimentally, the Brownian motion of the bead is characterised by the variance of the x or y coordinate from the centre-finding subroutine (see Section 3.1.1). However, since the measured extensions are not absolute, we cannot yet determine the forces, but a related quantity, the restoring stiffness. In this section, we first describe how variance is related to the pulling force, and also how the pulling force is related to the restoring stiffness. Then we explain how to determine the restoring stiffness from the Brownian motion.

### 4.2.1   Relating force to fluctuations

This system involves a bead which is being pulled up by a force proportional to $\nabla(\mathbf{m} \cdot \mathbf{B})$, but is constrained by the tension of a tethered molecule. Assume that the x, y and z orientation of the bead is fixed with respect to the direction of the field, as shown in Figure 2.7a. In an equilibrium situation, the pulling force and tension balance, and the bead is stationary. However, the bead is not at equilibrium since it resides within a thermal environment which causes the bead position to fluctuate. A force acts to restore the bead to its equilibrium position and is given by $F_r = -F_z sin\theta$.

We approximate the motion of the tethered bead as a harmonic oscillator, with a restoring force of the form $F_x = -k_x dx$. According to the equipartition theorem, the variance of bead position, $< dx^2 >$, and stiffness, $k_x$, are related to thermal energy by the following

expression for one degree of freedom:

$$\frac{1}{2}k_x < dx^2 > = \frac{1}{2}k_B T \tag{4.4}$$

where $k_B$ is Boltzmann's constant and $T$ is the temperature of the system in Kelvin. The angle of fluctuation does not exceed 6° when the system is aligned. So, we can approximate $F_x$ by $F_r$, and determine that $k_x = F_z/\ell$ (Fig. 4.5). Substitution of this expression into Equation 4.4 yields a useful relationship between the pulling force acting on the bead and direct observation of the position of the bead.

$$F_z = \frac{k_B T \ell}{< \delta x^2 >} \tag{4.5}$$
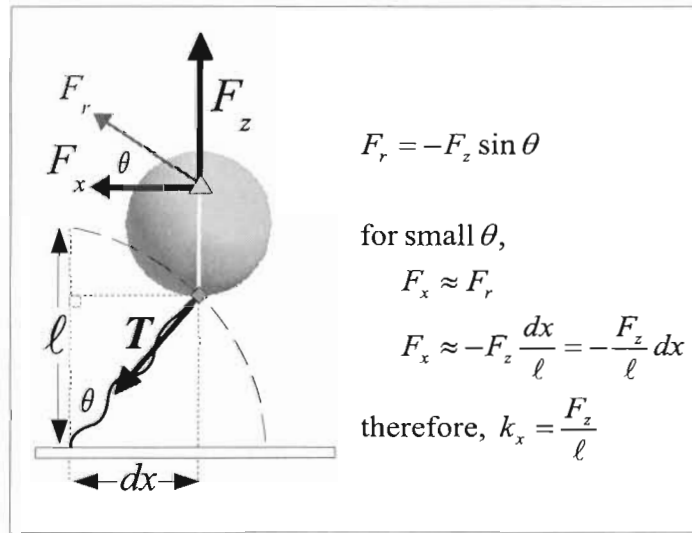


Figure 4.5: The restoring force, $F_r$, is the direct result of the upwards pulling force on the bead from the magnet pair, $F_z$. In the small angle approximation, we show that $F_x \simeq F_r = F_z dx/\ell$ for an angular displacement of $\theta$. Assuming a linear restoring force of the form $F_x = -k_x dx$, $k_x = F_z/\ell$. $\ell$ is the extension of the DNA molecule and $dx$ is the projected displacement from equilibrium on the x axis. The proportions represented in this figure are not to scale, and $\theta$ has been drastically exaggerated.

## 4.2.2 From fluctuations to stiffness

Our measurement of the DNA extension (end-to-end distance) is relative, so we cannot determine $F_z$ directly. Instead, the restoring stiffness, $k_x$, is what we first determine from the measured variance:

$$k_x = \frac{F_z}{\ell} = \frac{k_B T}{<\delta x^2>} \tag{4.6}$$

The procedure for obtaining the restoring stiffness from the measured bead positions is outlined in Figure 4.6. As with the determination of the z position of the bead, drift also affects the measurements of stiffness. If the bead is drifting in the xy plane, the calculated variance is an overestimate of the real variance. In order to correct for this, we use the same reference bead that is used in the z position determination (see section 3.3.1). We measure the (x,y) coordinates of the reference bead and tethered bead in each frame. The trajectory of the reference bead is low-pass filtered such that the general drift of the system is captured without high-frequency noise. Next, the low-pass filtered reference bead trajectory is subtracted from the tethered bead positions $(x_b, y_b)$ which should centre the fluctuations around the same value over the course of the experiment. Now, the variance of the x and y measurements for each magnet step can be reliably determined. We then apply Equation 4.6 to determine the restoring stiffness.

Note that since the tethered molecule is not a rigid object, the bead fluctuates in all three dimensions. The magnitude of the fluctuations in x and y is much larger than those in the z direction because the dominant force acts on the bead in the z direction. As $F_z$ becomes weaker, the fluctuations in z tend to increase leading to a larger z variance, along with larger x and y variances.

# 4.3 Experimental considerations when measuring forces

There are several experimental factors which affect measurements made on the magnetic tweezers that should be considered before analyzing data. How the sampling frequency and measurement duration are influenced by the correlation time of the bead motion is one such factor. The alignment of the magnet pair with respect to the optical axis is a factor which defines limitations on the magnets-to-bead distance, $\beta$. Also, anisotropy in the field produced by the magnet pair or magnetic particle distribution within the bead determine the
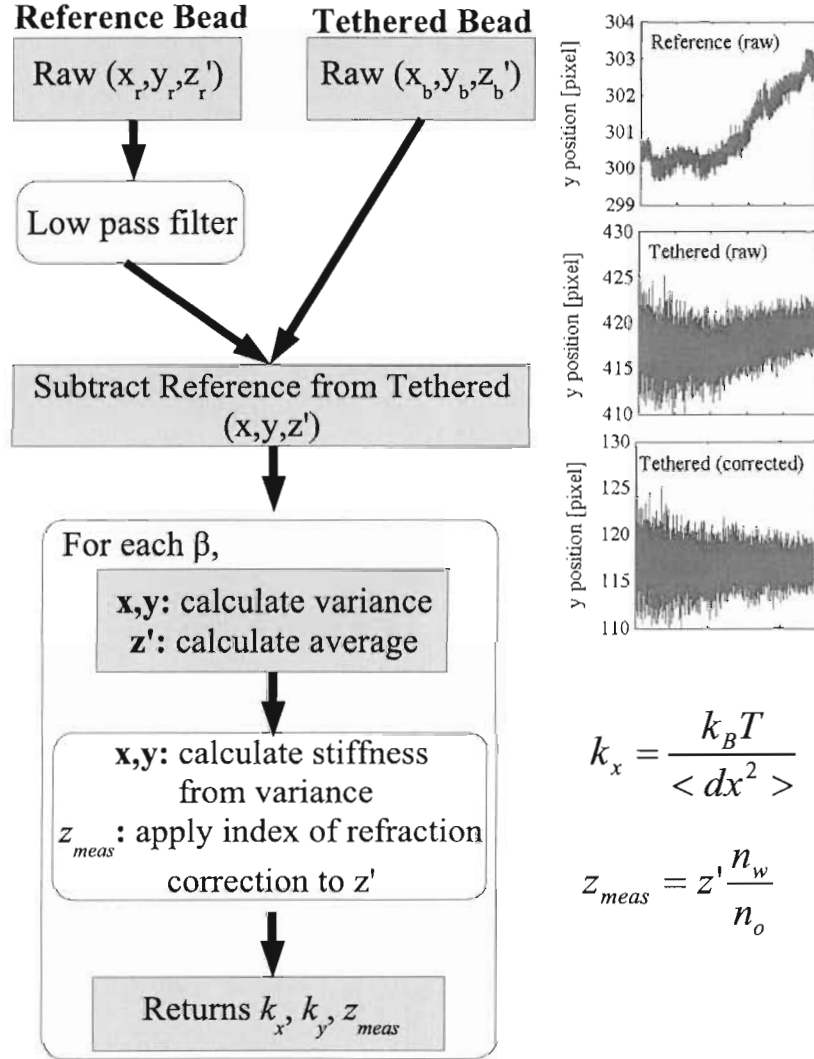
Figure 4.6: Analysis flowchart to determine the stiffnesses, $k_x$ and $k_y$, and bead height, $z_{meas}$, of an experiment in which the (x,y,z') positions of the bead are measured in each frame. z' is the apparent height of the bead which is then corrected for spherical aberration (Equation 3.3). For further details, see text.

axis (parallel or perpendicular to the field direction) along which to evaluate the variance of bead position.

### 4.3.1 Correlation time

The correlation time, $\tau_c$, associated with the Brownian motion of the bead represents the length of time required for the position of the bead to be randomized and can be calculated as follows [45]:

$$\tau_c = \frac{2\pi\gamma_0}{k_x} \tag{4.7}$$

where $\gamma_0 = 6\pi\eta r$ is the drag coefficient for a sphere, $\eta$ is the viscosity ($10^{-3}$ Pa.s) of water, $r$ is the radius of the bead (1.4 $\mu$m), and $k_x$ is the stiffness of the restoring force. The variance-based technique employed in our analysis gives the highest signal-to-noise ratio for $N$ measurements if these are each independent. This can be accomplished by taking measurements at least $\tau_c$ apart. If the measurements are not independent and are collected over durations that are not $\gg\tau_c$, the measured variance may underestimate the real variance. For the lower range of the stiffnesses that we expect ($k_x \sim 0.1$ pN/$\mu$m), $\tau_c$ is estimated to be $\sim$2 s. A 60-s measurement ($\sim 30\tau_c$) thus gives thirty independent measurements of the bead position. At higher forces, this number grows for a fixed sample period since $\tau_c$ decreases. In summary, the magnitude of the deviation of the measured variance from the real variance may depend on the length of time over which measurements are collected.

### 4.3.2 Alignment

Proper alignment of the magnet pair in the apparatus is very important to limit undesired lateral forces on the bead. Alignment can be tested by tracking the centre of a tethered bead while the magnets are rotated slowly ($\sim$ 0.01 rps). In the case of perfect alignment of the magnets along the rotational axis and tether point of the bead to the surface, the only force on the bead is in the positive z direction. When the system is aligned, rotation of the magnets does not cause the position of the bead to change (within a bead radius, see Figure 2.8c and e). However, when the magnets are not aligned, the bead is no longer in a symmetric field, which results in a net lateral force on the bead. The bead will feel a force in the xy plane whose direction and magnitude are dependent on the type of misalignment,

and the bead will trace out a curve if the magnets are rotated.

Misalignment can occur if both magnets do not trace out the same circle when rotated. This is the case when the magnet pair is shifted laterally with respect to the rotational axis, or the magnet surface is tilted with respect to the rotational stage. In both of these scenarios, there is always one magnet that is closer to a bead tethered at position $(0, 0, \beta)$. According to Equation 4.1, the bead is pulled towards in the direction of the gradient of the inner product between the magnetic moment of the bead and the field. Since the change in the field dominates this behaviour, the bead is attracted to the closest magnet and follows it as the magnet is rotated in a circle (Fig. 4.7a). The radius of this circle becomes smaller as $\beta$ increases. This type of misalignment has the strongest effect on the position of the bead.

It is only when the magnets are centred with respect to the rotational axis, but not centred with respect to the tether, that the effect of the other type of misalignment can be observed. When magnet pair is aligned, but the position of the tether is not, rotating the magnets once can lead to two revolutions of the bead. Figure 4.7b provides a pictorial understanding of the origin of this behaviour. As the magnets are brought closer to the bead, the radius of the trace increases as the forces in the xy plane exerted on the bead are stronger.

When the alignment is some combination of these two cases, the bead position trace will carry varying degrees of the idealized misalignments. Figure 4.8 shows a number of actual bead position traces taken for different magnet alignment scenarios. It is not our goal to make quantitative predictions about these traces but rather provide a qualitative measure of the system's alignment. The presence of circles in the bead position trace is indicative of a poorly aligned system. Once the magnets have been adjusted so that the trace is a more complicated pattern, then good alignment is near. The smaller the radius of a trace the better the alignment.

It is important to realize that the bead revolves around its tether position because of the forces caused by magnet misalignment, and rotates its magnetic moment because of the direction of the magnetic field and magnetisation anisotropy of the bead (see Section 2.3.3). Explicitly stated, the bead rotates only once with one rotation of the magnet pair. The bead can revolve more than once with the same rotation of the magnets.

With our calculations, we are able to determine the effect of a small misalignment of the magnet pair with respect to the tethered bead. Figure 4.9a shows the change in field and force when the magnets are offset by 1 mm in orthogonal directions. When the magnets
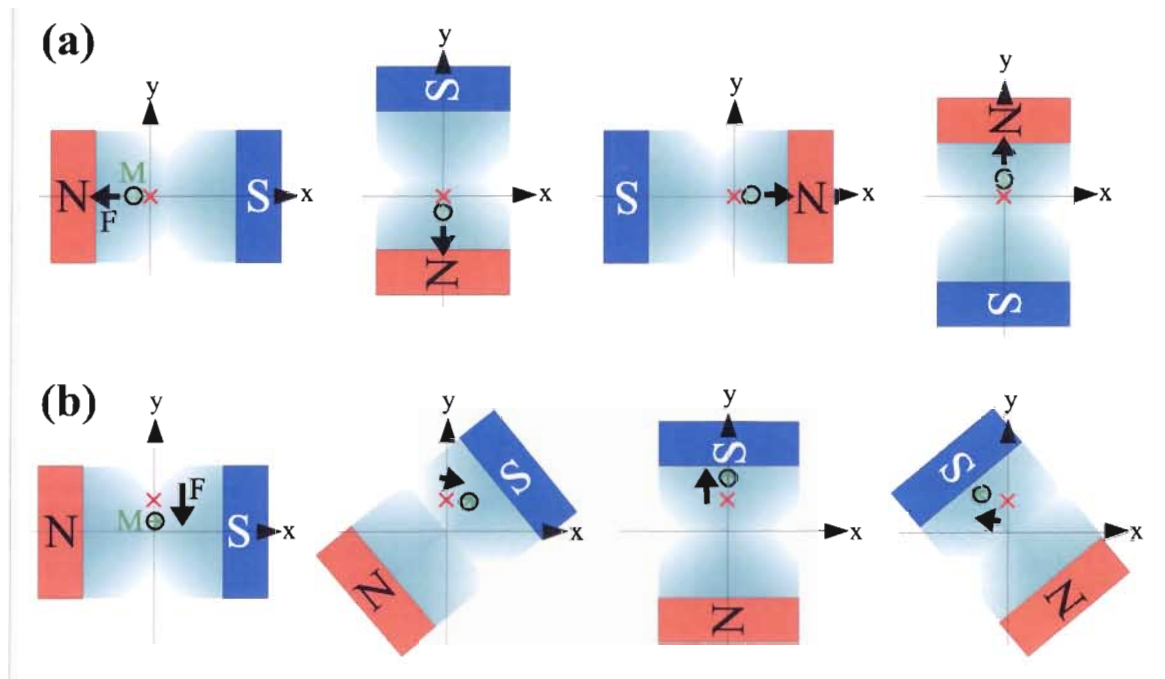
Figure 4.7: Misalignment of the tether, magnet pair, or rotational stage can be idealized into two observationally distinct situations. **B** is qualitatively depicted with the darker shades representing a stronger field. In this situation, the bead is attracted to the strongest field (gradient). (a) If the magnet pair (depicted with N and S poles) is not symmetric about the rotational axis while the tether position (red X) is centred, then one magnet will always be closer to the bead than the other. In this case, the bead (dark circle with bright magnetic moment vector) is attracted to the closer magnet. The offset of the bead from the tether position is not to scale and has been exaggerated for effect. The force vector is represented by a thick black arrow. So, if the magnet is rotated, the bead simply follows the closer magnet and traces out a single circle for a single rotation of the magnet pair. (b) In the second case, the magnets are centred with respect to the rotational axis but not the tether point. When the tether point is offset from the centre of the magnet pair, the bead feels an attractive force towards the closest magnet and a restoring force towards the midline of the magnets. This geometry can cause the bead to revolve twice while the magnets rotate once. Only half of a magnet rotation is depicted in part b of this figure.
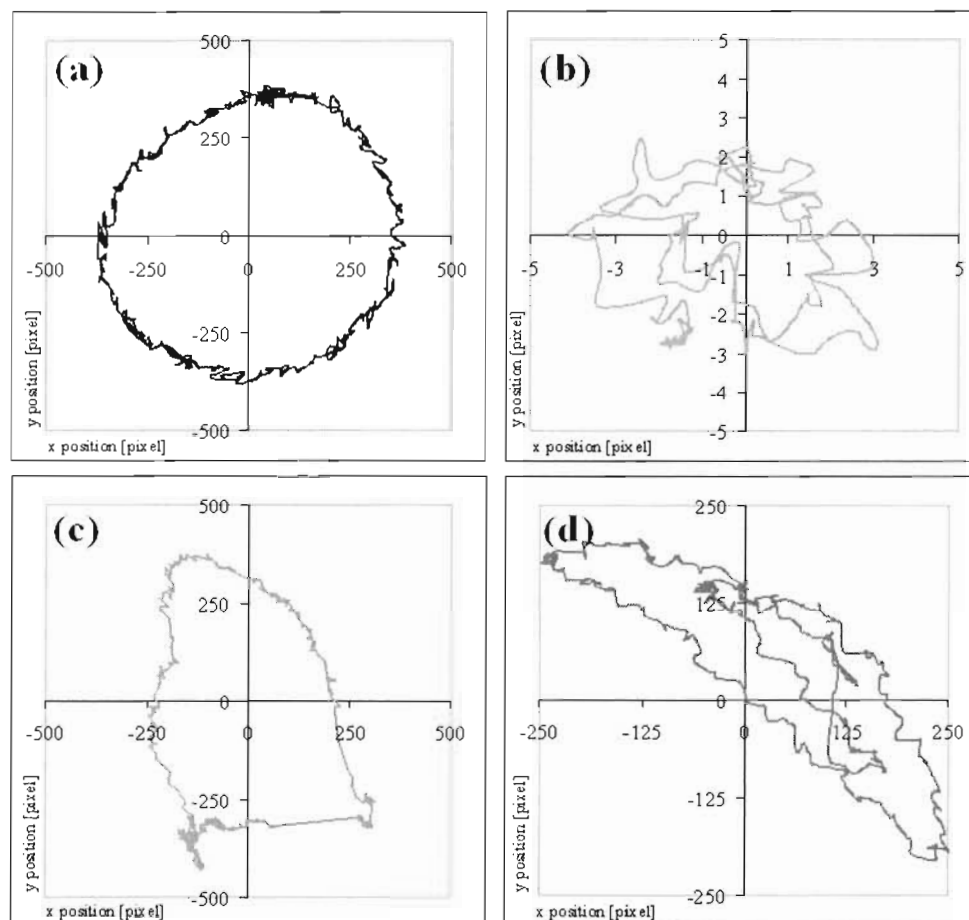
Figure 4.8: The quality of alignment between the magnet pair, the rotational stage and the optical axis can be determined by rotating the magnets and tracing the bead centre. (a) The bead traces out a single circle when the magnet pair is misaligned with respect to the rotational axis. (b) The bead traces out two 'circles' when the tether position is offset from the optical axis. (c) & (d) Examples of situations which involve both types of misalignment.
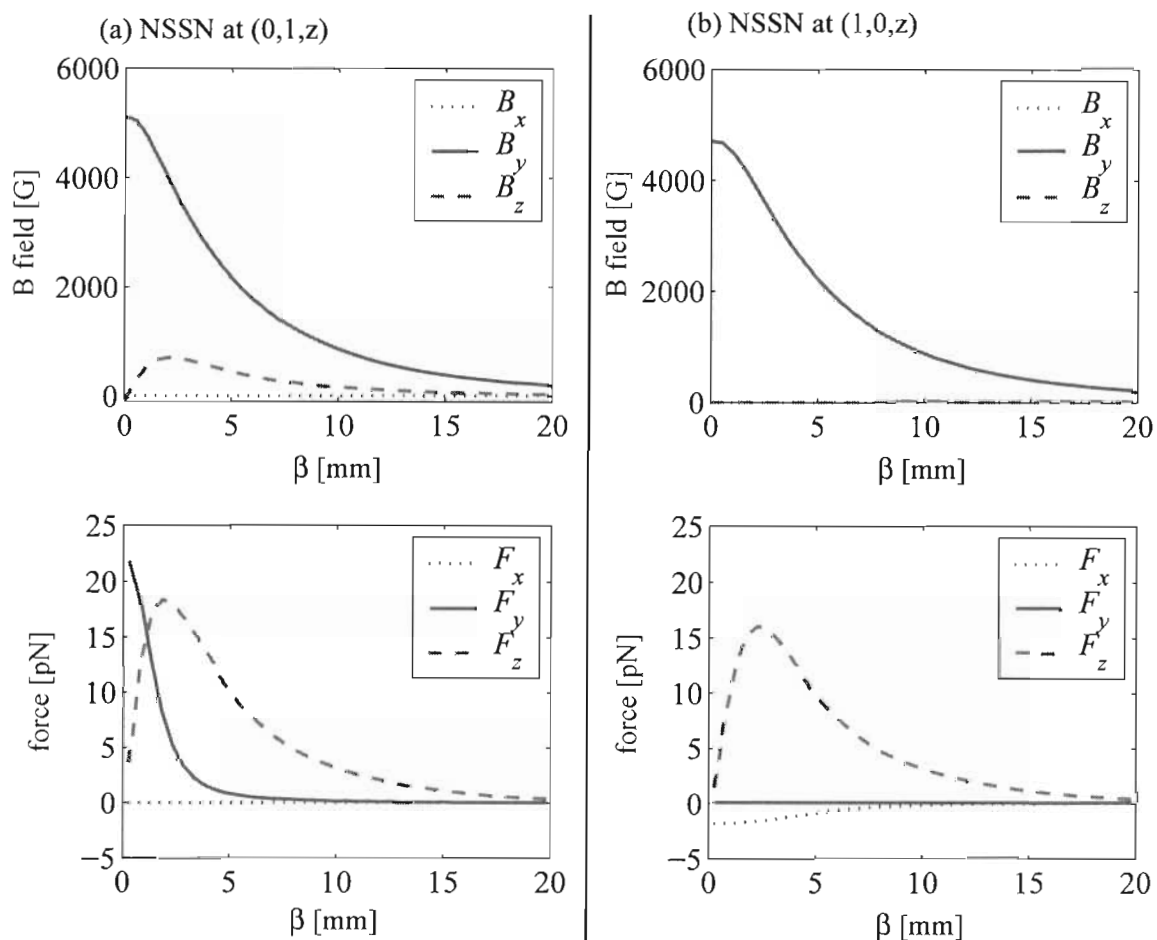
Figure 4.9: In the NSSN magnet configuration for $g = 5$ mm, the effect of a 1 mm misalignment of the magnet pair on the field and force is calculated. (a) If offset by 1 mm in the y direction, a force $F_y$ acts to pull the bead towards the closest magnet. (b) If the magnets are offset by 1 mm in the x direction, $F_x$ acts to restore the bead towards the centre. Note that $B_x$ is very small but nonzero. In both situations, the lateral force is very small compared to $F_z$ for magnets-to-bead height, $\beta$, greater than 7 mm.
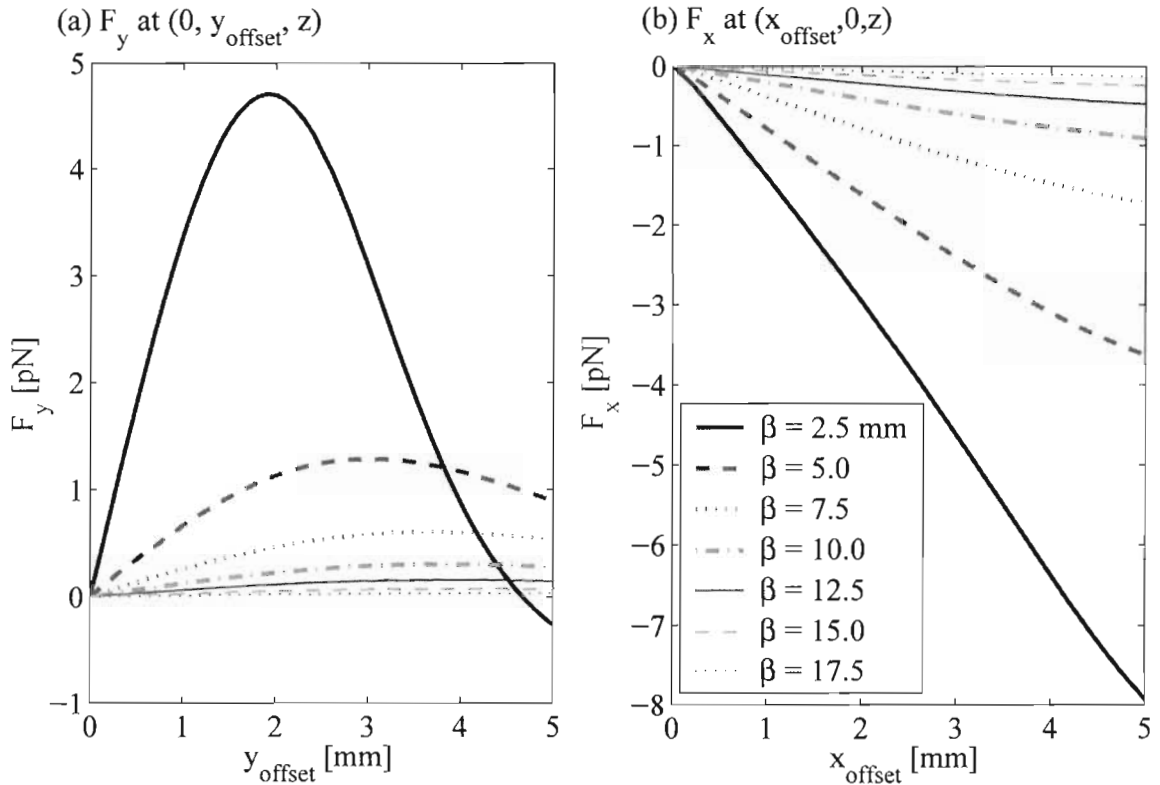
Figure 4.10: Calculated $F_y$ and $F_x$ as a function of the NSSN magnet pair offset for a number of different magnets-to-bead heights, $\beta$s, with $g = 5$ mm. The legend applies to both graphs. (a) When the magnets are misaligned along the y axis, a non-restoring force is produced. $F_y$ has a maximum at some offset distance which is dependent on the magnet height and gap size (not shown). (b) If the magnets are displaced along the x axis, a restoring force is generated. The magnitude of the force decreases with $\beta$.

are centred around (0, 1 mm, $\beta$), $B_z$ becomes nonzero which gives rise to a nonzero $F_y$. Note that $F_y$ for our magnet configuration is not a restoring force, as it is positive when the offset is also positive. Figure 4.9b illustrates the field and force generated from the magnets when centred around (1 mm, 0, $\beta$). In this case, the field does not change substantially but a weak restoring force in the x direction is produced. Comparing the two cases, an offset in the y direction produces much stronger effects on the bead than an offset in the x direction. However, both 1 mm misalignment situations do not produce significant forces on the bead in the x and y directions compared with $F_z$ when the magnets are at least 7 mm away (Fig. 4.10).

The angle between the stretched DNA and surface depends on the relative strengths of $F_x$, $F_y$ and $F_z$ on the bead, and hence on the height and alignment of the magnets relative to the tether point. In the presence of nonzero $F_y$, the bead height is less than the total DNA extension. The change in position of the bead for small magnet-to-bead distances has been verified by observation. At the time of the experiments presented here, the magnetic tweezers were within 1 mm of perfect alignment. The data presented in this thesis are limited to situations in which $\beta$ is greater than 7 mm.

### 4.3.3 Variances perpendicular and parallel to the field

Experimental data has consistently shown that the variance of the bead position measured perpendicular to the direction of the field is not equal to the variance parallel to the field direction ($\sigma_\perp^2 \neq \sigma_\parallel^2$) (Fig. 4.11). The origin of this asymmetry is the focus of ongoing investigations in our group.

One possible explanation is based on the field generated by the finite geometry of the magnet pair. The **B** field from infinite magnets would be uniform over the xy plane for a particular $\beta$. However, since the magnets are finite, **B** is not constant across this plane. These differences gives rise to small lateral forces: a non-restoring force in the direction parallel to the field, and a restoring force perpendicular to the field. This situation is akin to misalignment, but acts only as a perturbation to the dominant pulling force in the z direction. It is possible that these small, asymmetric perturbations are significant enough to be manifest as observable differences between variances in orthogonal directions. However, it was determined through calculations that thermal fluctuations are more than enough to

overcome the difference in energies between the bead position along the x and y directions, therefore, field gradients in the xy plane do not seem a likely explanation for asymmetric variances.

The difference between $\sigma_\perp^2$ and $\sigma_\parallel^2$ can also be explained by a difference in effective tether length of the fluctuating bead in the two orthogonal directions. The bead may have a preferred orientation in the plane parallel to the magnetic field resulting from the interference between the induced magnetic fields of the ferrimagnetic particles within the bead (demagnetising field). This can occur if the distribution of the magnetic particles is anisotropic. So, in the direction parallel to the field, the anisotropy constrains the orientation of the bead such that it fluctuates as in Figure 4.12a. The effective tether length, in this case, is the extension of the DNA, $\ell$. If the bead is free to rotate without changing its energy, as it may in the direction perpendicular to the field, then the effective tether length for motion in the perpendicular direction is $\ell + r$ and fluctuations are of the form shown in Figure 4.12b. Currently, no conclusive argument has been made for the effective tether length in the direction perpendicular to the field [46]. Therefore, we explore both of these possibilities when trying to extract the persistence length, $L_p$, and offset, $z_0$, from the data.

Further testing is required to understand the origin of the asymmetric variances. One appropriate test would be to increase the lateral offset of the magnet pair, and observe the
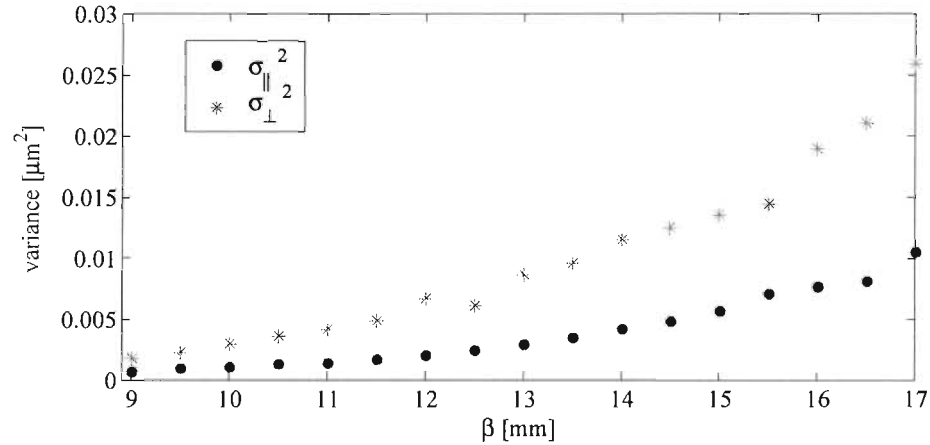


Figure 4.11: The variances measured parallel and perpendicular to the direction of the field ($\sigma_\parallel^2$ and $\sigma_\perp^2$, respectively) are consistently different. Here, they are plotted as a function of magnet height, $\beta$.
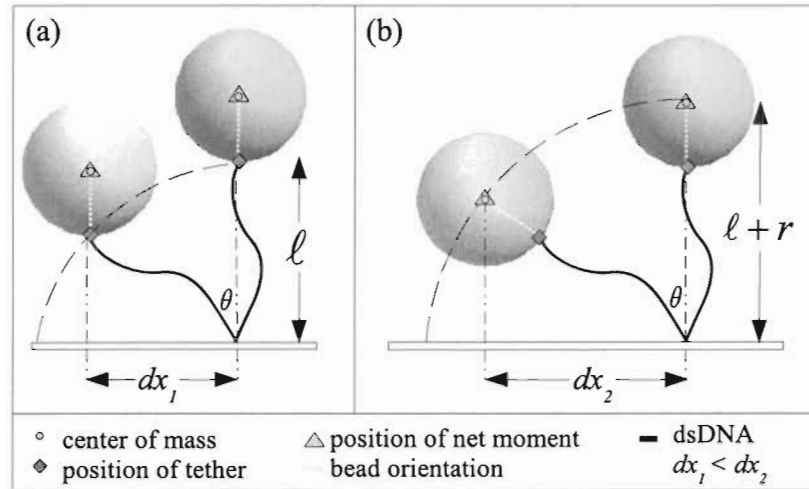
Figure 4.12: Effective tether length of a fluctuating bead. (a) The orientation of the bead is maintained with respect to the field. The effective tether length is the DNA extension, $\ell$. (b) For the same fluctuation angle, $\theta$, the bead is free to rotate about the tether point. The effective tether length is the DNA extension plus the radius of the bead, $r$.

effect on the variances parallel and perpendicular to the field. Another test would determine the ratio between $\sigma_\parallel^2$ and $\sigma_\perp^2$ for a number of different DNA molecules with different lengths.

## 4.4 Force-extension curves

This section discusses the steps involved in generating a force-extension curve for our data. The process of determining the offset between relative and absolute DNA extension measurements is explained in detail. This offset is required when calculating the pulling force from the restoring stiffness. We describe attempts to pull on a 3.96-$\mu$m-long dsDNA molecule, measure the force as a function of DNA extension, fit to the worm-like-chain model [27] and extract the persistence length, $L_p$.

## 4.4.1 The worm-like-chain model

The worm-like-chain model (WLC) has been used extensively to describe the elastic proper-
ties of semi-flexible polymers (Fig. 4.13a) [27, 47]. It has been fit to force-extension curves
generated from pulling experiments on dsDNA conducted with optical tweezers [15, 28],
the atomic force microscope [29], flow fields [30], and magnetic tweezers [5, 27] to extract
the persistence length, $L_p$. Briefly, the persistence length is a measure of the contour dis-
tance over which the direction of the tangent to the molecular backbone is correlated. In
other words, $L_p$ is related to the rigidity of a polymer. The smaller the value, the more flex-
ible the molecule. Since $L_p$ has been determined for dsDNA in standard buffer conditions,
the value we obtain from our fits can be compared with this standard.

The WLC model states that the force and extension of the molecule are related in the
following nonlinear manner:

$$F = \frac{k_B T}{L_p} \left( \frac{1}{4(1 - \frac{\ell}{L})^2} - \frac{1}{4} + \frac{\ell}{L} \right) \tag{4.8}$$

where  $k_B T$  is the thermal energy,

$L_p$  is the persistence length (53 nm in our buffer conditions [15]),

$\ell$  is the absolute DNA extension (end-to-end distance),

and  $L$  is the contour length of the molecule (3.96 $\mu$m in our experiments).

Since our measured z values ($z_{meas}$) are relative, we cannot fit our data to the traditional
WLC model (Equation 4.8). The absolute extension of the DNA is required to calculate the
force from Equation 4.5. For the restoring stiffnesses measured parallel to the direction of
the field, $k_{\parallel}$, we include an offset, so that the absolute extension is given by $\ell = z_{meas} + z_0$.
Then we fit the stiffness, $k$, to the following expression to obtain values for $L_p$ and $z_0$:

$$k = \frac{F_z}{\ell} = \frac{k_B T}{L_p(z_{meas} + z_0)} \left( \frac{1}{4(1 - \frac{z_{meas} + z_0}{L})^2} - \frac{1}{4} + \frac{z_{meas} + z_0}{L} \right) \tag{4.9}$$

where  $z_{meas}$  is the measured height of the bead, corrected for drift using the
reference bead and corrected for the index of refraction mismatch,

and  $z_0$  is the offset from our relative measured heights to absolute extensions.
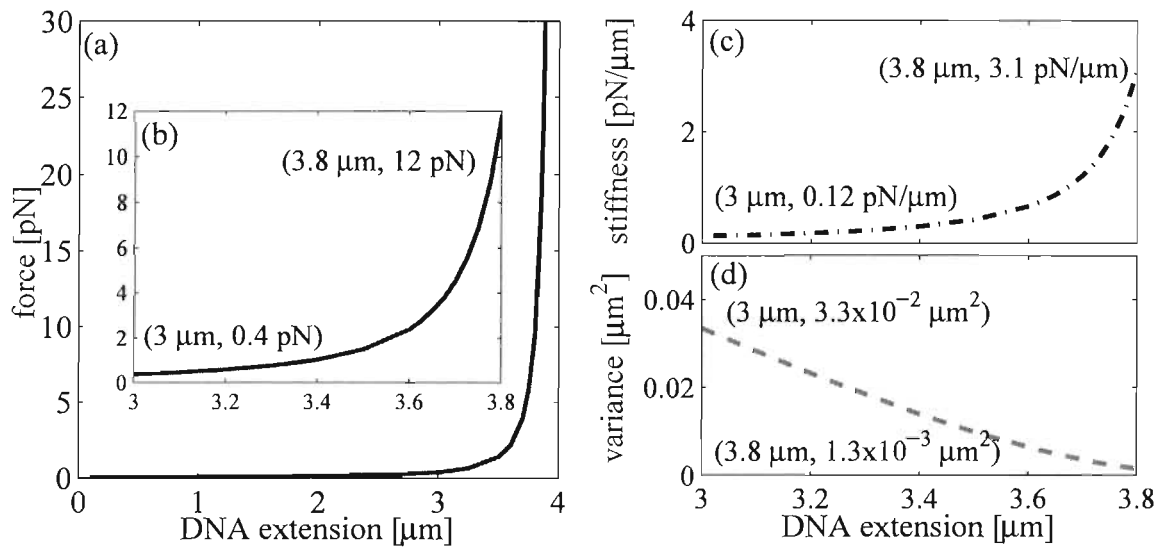
Figure 4.13: (a) The force-extension curve arising from an idealized worm-like-chain model with $L = 3.96$ $\mu$m and $L_p = 53$ nm. (b) The inset graph is a subsection which roughly corresponds to the region experimentally accessible with our magnetic tweezers apparatus in its current configuration. (c) The restoring stiffness-extension curve of the same region described in part b. (d) The variance-extension curve of the same region described in part b. A uniform field perpendicular to the pulling direction was assumed for these calculations.

For the restoring stiffnesses measured perpendicular to the directions of the field, $k_\perp$, we must consider both Equation 4.9 and the situation in which the effective tether length is $\ell + r$, where $r$ is the radius of the bead. We then obtain another modified form of the WLC model suitable to fit to the measured restoring stiffnesses:

$$k = \frac{F_z}{\ell + r} = \frac{k_B T}{L_p(z_{meas} + z_0 + r)} \left( \frac{1}{4(1 - \frac{z_{meas} + z_0}{L})^2} - \frac{1}{4} + \frac{z_{meas} + z_0}{L} \right) \qquad (4.10)$$

The fitting parameters are $z_0$ and $L_p$. At this point, we have already obtained the persistence length for this particular data set. However, the literature does not typically present extensions with respect to stiffnesses, but to force. Ideally, we can fit $F_z$ versus $\ell$ to the traditional WLC model (Equation 4.8) to acquire the equivalent $L_p$ as from the fit to Equation 4.9 (or Equation 4.10). However, we have shown through simulations that as the noise of the data increases, the $L_p$ values from the fit decreases. Also, $L_p$ from the WLC model of Equation 4.8 decreases faster than when fit to Equation 4.9. In this thesis, we quote the $L_p$ and $z_0$ obtained from fitting to the adapted WLC model for restoring stiffness (Equation 4.9 or, where appropriate, 4.10).

### 4.4.2 Single tether?

During our initial experiments, we noticed that the variance versus extension data showed qualitative resemblance to stretching DNA (Fig. 4.13). However, the values of stiffness measured are an order of magnitude larger than expected, and therefore persistence lengths resulting from fitting to Equation 4.9 are much less than expected (Fig. 4.14). We have concluded that multiple tethers are the likely cause of these discrepancies because the stiffness measured in subsequent experiments approached those expected for a single tether when the ratio of DNA strands to beads was decreased.

The radius of gyration, $R_g$, of a 4-$\mu$m dsDNA molecule is about 270 nm [48]. From this, the number of molecules that would cover the surface of a bead with known radius can be easily estimated: about 100 molecules for our 2.8-$\mu$m-diameter bead. To promote the formation of single tethers, we require a surface concentration of bound molecules such that there is only one for each region of the bead that comes into close contact with the surface. The bead lingers close to the surface for many minutes, so all the free ends of the
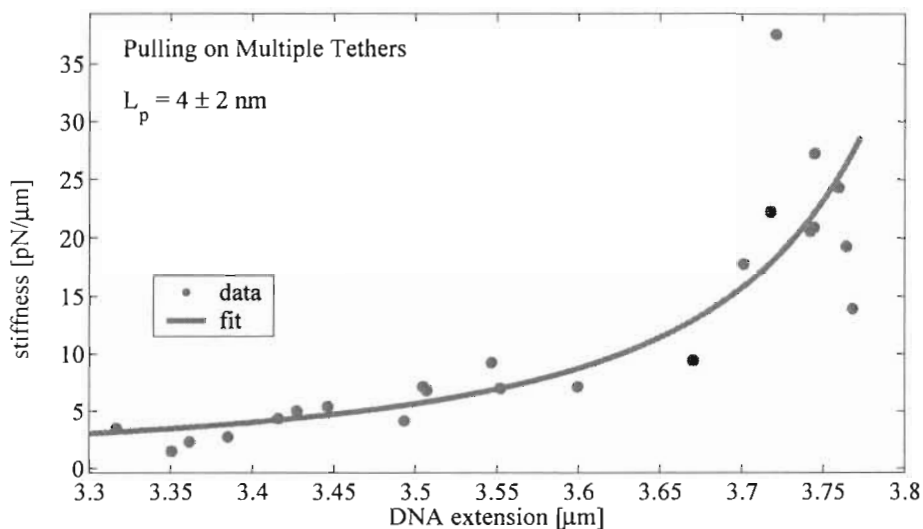
Figure 4.14: Data from a pulling experiment in which the bead was likely bound by multiple tethers. The data fits well to Equation 4.9, but gives an $L_p$ much smaller than expected. The stiffness values are an order of magnitude greater than expected.

DNA within the region will likely bind to the surface. We have found that a ratio of ten molecules per 2.8-$\mu$m-diameter bead provides mostly single tethers.

The measured variances of the bead position reflect the number of tethers holding the bead to the surface. So, it is useful to calculate the range of variances expected from the forces that will be applied to a single molecule. We expect to measure variances of 3.3 $\times 10^{-2}$ to 1.3 $\times 10^{-3}$ $\mu$m$^2$ (Fig. 4.13d). This range will serve as a guide when selecting a bead on which to perform a measurement. The LabVIEW control program is written to estimate the variance of the most recent 100 frames. For a bead tethered by a single molecule at low forces, the variances measured in the x and y directions should be roughly the same and fall within the expected order of magnitude. If the bead in question does not satisfy these criteria, then it is most likely connected to the surface by more than one tether.

### 4.4.3 Our stiffness-extension data

Previous studies on stretching DNA have determined that its persistence length is dependent on the ionic environment [28]. The cations in the buffer shield the negatively charged DNA

backbone from itself. In buffers containing 10 mM Na$^+$, $L_p$ was found to be $\sim$47 nm, while in a 4 mM Mg$^{2+}$ buffer $L_p$ was determined to be $\sim$40 nm [28]. To compare our results with literature values of $L_p$, we used the following buffer: 150 mM NaCl, 10 mM Tris, 1mM EDTA, pH 8. The accepted value for $L_p$ in this buffer is 53 $\pm$ 2 nm [15].

A typical measurement sequence in our instrument involves collecting (x,y,z) positions of a bead for duration $t$, while the magnet pair is held at a fixed height. The magnets are then stepped to a new height, and another set of (x,y,z) data is taken. The data collected at each step are analyzed to give three values: a relative DNA extension, $z_{meas}$, and the restoring stiffness along each axis of the image, $k_{||}$ and $k_\perp$ (Fig. 4.6). The difference between the absolute and measured relative extensions, $z_0$, and the persistence length can be determined by fitting to Equation 4.9 with the MATLAB Curve Fitting Tool. If required, $z_0$ can then be added to $z_{meas}$ to obtain the absolute extension, $\ell$ and the force calculated from $F_z = k\ell$.

Figure 4.15 provides evidence that our magnetic tweezers apparatus and analysis algorithms yield results which can be similar to other studies. In the direction parallel to the field, we have fit stiffness data, $k_{||}$, to Equation 4.9. Because the origin of the asymmetric variance remains unknown, we have fit $k_\perp$ to both Equation 4.9 and 4.10. The resulting values for $L_p$ and $z_0$ are also presented in Figure 4.15. The data obtained from the first iteration of our magnetic tweezers suffers from much noise, so the $L_p$ values should not be taken to be precise. A section of the following chapter discusses improvements that can be made to our instrument that would reduce the noise in our acquired position data. With some improvements to the apparatus and more statistics, these data indicate that single-molecule extension experiments are possible with our magnetic tweezers.

## 4.5 Force as a function of $\beta$

The pulling force acting on a molecule can be determined from the variance of the bead position using the analysis method outlined in the previous sections of this chapter. In this section, we discuss the forces as a function of the magnets-to-bead distance, $\beta$, compared to the calculated results for an *average* bead.

Figure 4.16 shows the measured force as a function of $\beta$ plotted against the calculated results for an average bead and beads with different percentages of the total force of an average bead. The force is calculated by multiplying the restoring stiffness by the effective
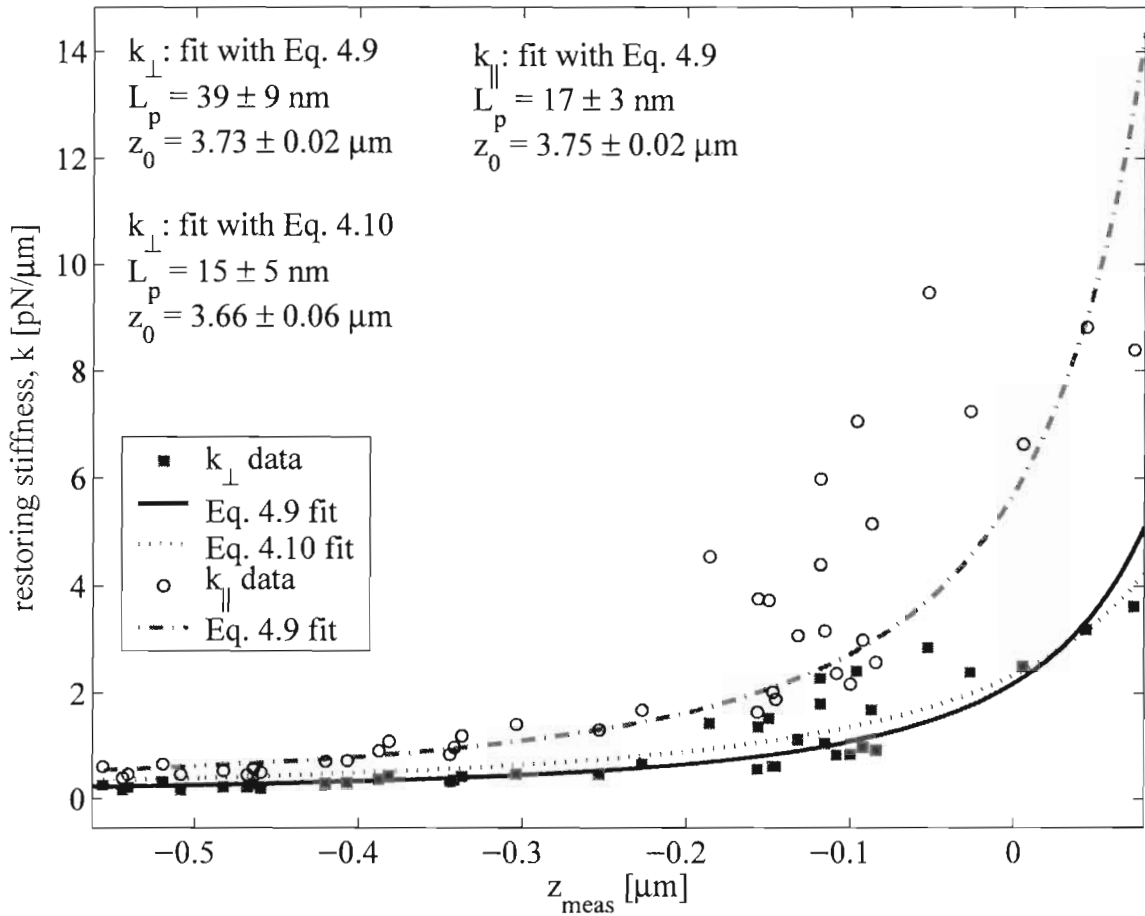
Figure 4.15: Stiffness-$z_{meas}$ data for a 3.96-$\mu$m-long dsDNA molecule collected for two consecutive pulls in both the directions parallel and perpendicular to the field. The magnets were brought from 7.5 mm to 17 mm away from the chamber surface. Each data point is based on 500 images at a frame rate of 15 Hz from which the bead variances in the direction either parallel or perpendicular to the field were taken. The data have been corrected for drift using a reference bead. The index of refraction mismatch correction has been applied (see Section 3.3.2). Both $k_{\|}$ and $k_{\perp}$ were fit by Equation 4.9 for an effective tether length of $\ell$. $k_{\perp}$ was also fit by Equation 4.10 for an effective tether length of $\ell + r$.

tether length, either $\ell$ or $\ell + r$. The induced magnetic moment expected from an average bead of this type (Dynabeads$^{TM}$ Protein G superparamagnetic) is calculated from the manufacturer's bulk magnetisation and density data (Fig. 2.6) [39]. The range of $\beta$ for this particular experiment is 7.5 mm to 17 mm, and is based on the same data as shown in Figure 4.15. Due to limitations in aligning the system, were were not able to access the region of $\beta$ for which a decrease in force is expected as $\beta$ is decreased.

The measured force values do not quantitatively agree with the expected values. However, we notice that, qualitatively, they share the same trend.

It is not surprising that there is variability in the forces achieved from bead to bead, since the quantity of magnetic material is not consistent among beads. Beads with different ferrimagnetic content will have different induced magnetic moments and will thus generate different forces. For this particular bead, the force values are closer to a bead which has 150% of the force expected for an average bead. Other groups using similar beads have found as much as 30% variability in the amount of force exerted [8, 9].

Another explanation for the deviation from the expected force values involves the correlation time of the system. As mentioned in Section 4.3.1, at our expected lowest accessible force, the time between independent measurements is about 2 seconds. The time between our measurements is 0.067 s, since data were acquired at 15 Hz. Thus, our current measurements have likely underestimated the true variance of the system for large $\beta$. This ultimately leads to an overestimation of the force in this region of low force. We plan to address this issue in future experiments.

Although there still remains a deviation between the measured and expected forces on a superparamagnetic bead, we have addressed and accounted for some of the causes. Further investigation is required to uncover the remaining causes of the difference.
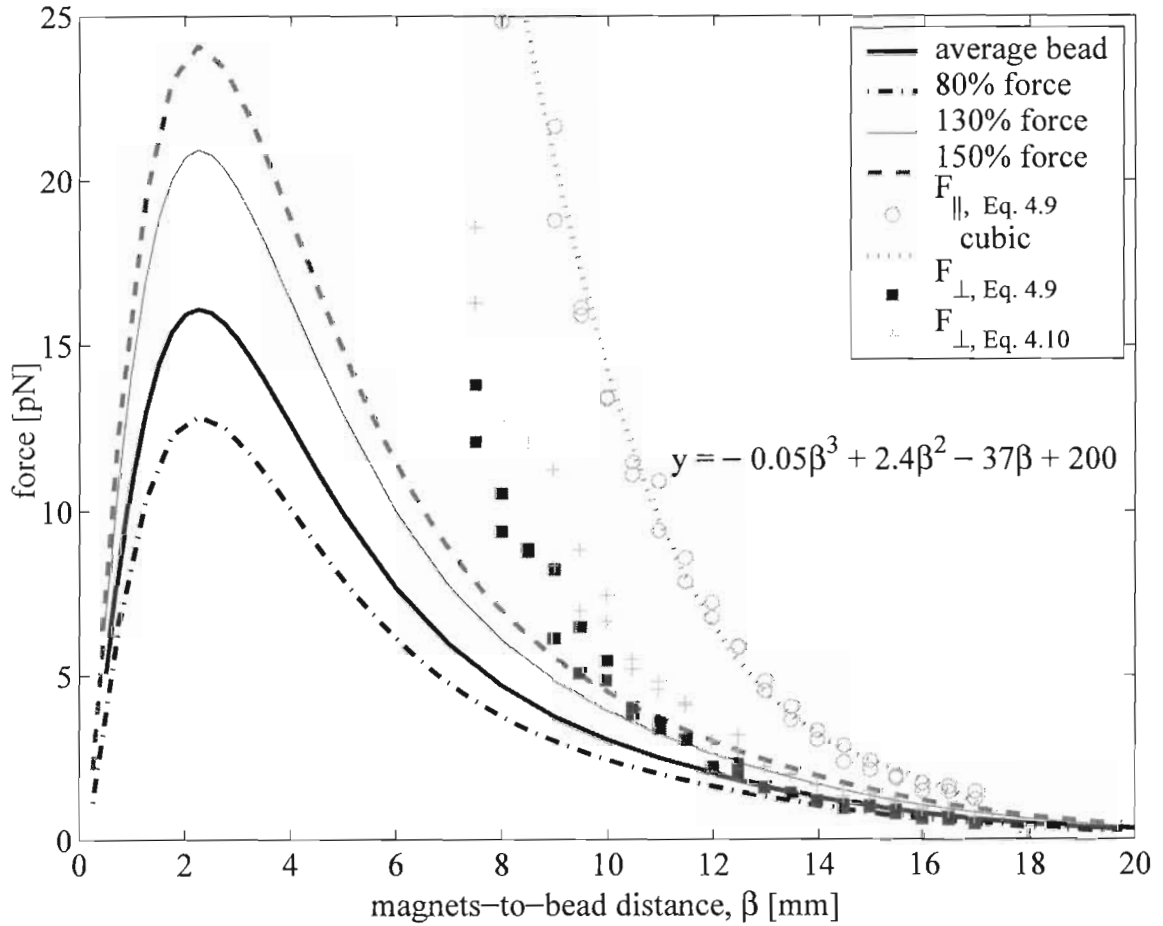
Figure 4.16: The experimentally determined forces as a function of magnets-to-bead distance, $\beta$, are compared to the expected forces calculated for an average bead, and beads with different percentages of the force of an average bead. The data are taken from measurements of bead variance in the directions parallel and perpendicular to the field. Explicitly stated, experimental forces are given by: $F_{\|,Eq.4.9} = (k_{\|})(z_{meas} + z_0)$, $F_{\perp,Eq.4.9} = (k_{\perp})(z_{meas} + z_0)$ and $F_{\perp,Eq.4.10} = (k_{\perp})(z_{meas} + z_0 + r)$. $F_{\|,Eq.4.9}$ is well fit by a third-order polynomial.

# Chapter 5

# Future work and summary

## 5.1 Future work

In this section, we discuss suggested improvements to be made to the current system, and some of the questions that remain to be addressed before collagen can be pulled and twisted.

**Apparatus and software interface**

It is crucial for the z position resolution of the bead that the objective lens be stepped by known amounts during calibration. Our ability to control the step size is limited by the objective height controller. The change in height of the objective lens relies on a Z-axis Focus Drive that is connected to the fine focus knob of the microscope. The Focus Drive is capable of a smaller rotational step than the sensitivity of the fine focus knob. If the objective lens were mounted directly to a piezo driver, by-passing the rack and pinion construct of the microscope, the resolution of height measurements would improve.

If the magnetic tweezers is used to exert forces greater than 5 pN, proper alignment between the optical and rotational axis is critical. The weight and size of the rotational stage make it difficult to mount and position precisely. The current set-up only allows rough changes to the position of the rotational stage with respect to the optical axis. If mounted to a sturdy, micrometer-controlled xy-platform, the rotational stage could be aligned to higher precision. Since the magnet holder expands and contracts with changes in temperature, an easily adjustable yet precise mount for the rotational stage would also decrease the set-up

time before each use of the magnetic tweezers.

Replacing the oil-immersion objective lens with a water-immersion variety would eliminate the correction for the index of refraction mismatch.

The reference bead subtraction is a valid and simple step to remove instrumental drift from the system. However, it is better to remove the source of the drift, if possible. We suspect that there is correlation between temperature fluctuations within the room and the (x,y,z) position of beads stuck to a surface. Protection from air currents, or drafts, can be accomplished by enclosing the instrument in a box. Furthermore, if the box is temperature controlled, then the magnitude and rate of the already small changes in temperature within the laboratory would also decrease. Controllers, computers, fans and other devices that heat or cool should be kept as far away from the instrument as possible.

Currently, the analysis software is set up only to analyze one bead, meaning that the (x,y,z) positions of the tethered bead and the reference bead are obtained from sequential analysis of saved images. A multiple-bead tracking system could be incorporated into our LabVIEW software in which the position of more than one bead can be analyzed and recorded simultaneously.

**Before collagen studies**

The magnetic tweezers is capable of not only pulling, but also twisting single molecules. However, we have not yet explored, experimentally or theoretically, the abilities and limitation of our instrument to apply torque. Although the maximum torque exerted on a molecule can be calculated theoretically, it is specific to the magnetisation distribution within the bead, and a general value cannot be quoted. So far, literature reports suggest that twisting of DNA with a superparamagnetic bead has not been limited by a maximum torque [49]. However, the torque required to denature a single molecule of collagen may lie in a different range.

Another concern stems from the short length of a collagen molecule ($\sim$300 nm). When a 3 $\mu$m bead is tethered by such a short molecule, the Brownian motion of the bead is influenced by the presence of a semi-infinite surface, the chamber. Since the analysis of the force exerted on the molecule relies on the magnitude of the position fluctuations, these surface effects must be determined prior to obtaining meaningful collagen pulling and twisting data.

## 5.2 Summary

This thesis has presented the development and characterisation of a magnetic tweezers instrument to be used in single-molecule manipulation studies. The instrument components and analysis techniques are discussed in detail, including the steps required to obtain DNA extensions from bead heights, and to extract forces from the variances of the bead position. The values of the persistence length of dsDNA acquired with our instrument are approaching the accepted values.

In constructing the instrument, a deeper understanding of the underlying physical principles of the apparatus was gained. New insight into the orientation and rotation of a tethered bead allowed for development of intuition regarding the motion of the bead with respect to the direction and gradients of the magnetic fields. Furthermore, after successful modeling of the magnetic fields for a magnet pair, the expected forces on a superparamagnetic bead were calculated and determined experimentally.

The current level of understanding has proven to be enough to operate the magnetic tweezers and obtain data that is in agreement with results from other techniques. However, it will still benefit present and future users of the magnetic tweezers when subtleties within the analysis and the underlying physical principles of the instrument are explored and documented.

# Appendix A

# List of apparatus components

Table A.1: Apparatus component information

| Part | Details | |
|---|---|---|
| *Newport Vibration Isolated Workstation* | model | VH3648W-OPT25-01-01-NN-NN-N-1-N-N-N |
| *Nikon inverted microscope* | model | TE2000S |
| | objective lens | 100x oil-immersion Plan Apo DIC H, NA 1.4 |
| *PI Linear positioner* | model | M-126.DG |
| | controller | C-862.00 |
| | minimum step | 0.1 $\mu$m |
| | load capacity | 20 kg |
| | range | 25 mm |
| *Danaher Motion Rotation Stage* | model | DRT-100-E2-L-LN2-K |
| | amplifier | Kollmorgon Servostar CD CE03250 |
| | PCI card | Galil 1810 |
| *Point Grey Camera* | model | B & W Flea CCD |
| | resolution | 640 x 480 pixels |
| | | Continued on next page |

**Table A.1 – continued from previous page**

| Part | Details | |
| --- | --- | --- |
| *Z-axis Focus Drive* | model | Digipot |
| | controller | Prior Optiscan I |
| | minimum step | 0.1 $\mu$m |
| *Linkam Stage Heater* | model | THN-60-16 |
| | controller | DC 60 |
| | range | ambient to 60 °C |
| | resolution | 0.1 °C |
| *Rare earth magnets* | material | NbFeB |
| | size | $\frac{1}{2}$" cube |
| | source | K and J Magnetics, Inc. |
| *Halogen 100W lightbulb* | model | Osram HLX 64623 |
| | voltage | 12 V |
| *Dell Dimension 3000 series* | processor | Pentium 4, 2.8 GHz |

# Appendix B

# Preparation of torsionally constrained DNA

For magnetic tweezers experiments involving torque, it is required that dsDNA be torsionally constrained at both the chamber surface and the bead surface to prevent undesired release of induced torque. Unless nicked, dsDNA does not contain any structures which freely swivel. Torsional constraint is achieved by binding each end of the DNA with at least two ligand-receptor interactions offset from the end of the molecule.

The following protocol has been adapted from [50] to prepare differentially labeled molecules with multiple labels on each strand. To label a DNA strand at more than one location requires a technique that allows multiple labeled nucleotides to be incorporated into a dsDNA patch, such as polymerase chain reaction (PCR). The final product consists of one multiply labeled patch (∼1 kb) followed by a region of unlabeled DNA, and then a differently labeled patch as shown in Figure B.1.

Two distinct 1 kb segments are PCRed with a small percentage of labeled nucleotides, such that one 1 kb fragment is labeled with multiple biotin (bio) molecules and the other with multiple dioxigenin (DIG) antigens. The template for the PCR is λ-DNA (NEB, N3011S) and the primer oligonucleotides (Sigma-Aldrich) amplify the λ-DNA from site 18951 to 20100 (bio-1kb) and 45595 to 46693 (DIG-1kb). One end of each of the 1 kb pieces is cleaved with the restriction endonucleases *NgoMIV* (bio-1kb) and *NarI* (DIG-1kb) leaving 1 kb pieces with sticky ends with a four (3' GGCC 5') and two (3' CG 5') basepair overhang, respectively. All restriction enzymes used in this protocol were obtained from

New England Biolabs.

A region of $\lambda$-DNA can also be selected to make up the central unlabeled sequence of the DNA construct. Many lengths of DNA can be made by selecting the appropriate set of restriction endonucleases. For example, $\lambda$-DNA can be cleaved at site 39888 by *XmaI* and site 43392 by *AclI*, and then purified to yield a 3.5 kb strand ($\sim 1 \ \mu m$). The generated sticky ends (5' CCGG 3' and 5' GC 3', respectively) match the ends of the digested 1kb fragments and can be ligated together with T4 DNA ligase (Invitrogen, 15224-017).

An additional safeguard for proper ligation occurs if all four endonucleases are present in the ligation reaction. Recognition sequences of endonucleases are often palindromic. This means that when two of the same strands ligate, the endonuclease that originally generated the sticky end will, again, cleave the two strands. However, the enzyme will not cleave the correctly ligated 1 kb - 3.5 kb construct since the recognition sequence is no longer formed.
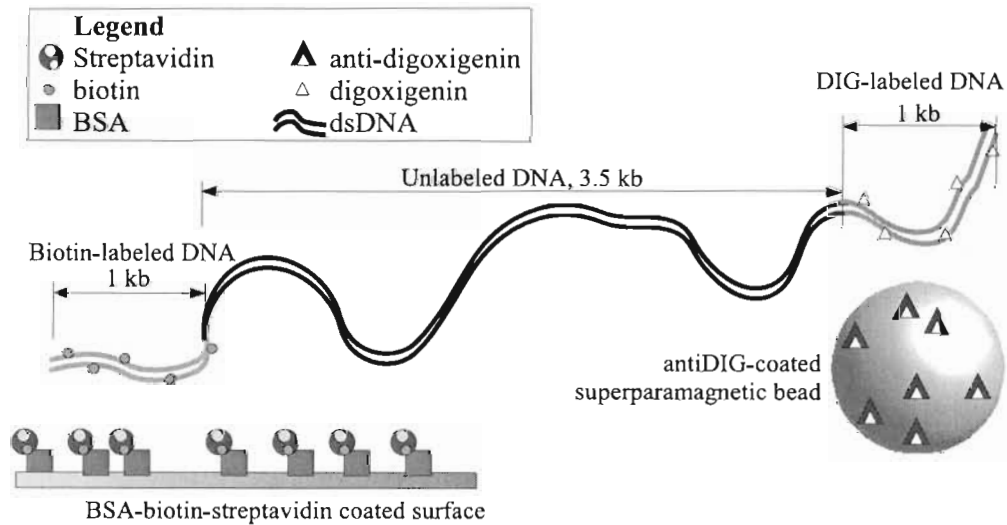


Figure B.1: Schematic of torsionally constrained sample required for twisting measurements on DNA. The DNA construct consists of an unlabeled sequence of known length sandwiched between two 1 kb segments with multiple labels (biotin and digoxigenin, respectively). The biotin-end of the DNA is attached to the streptavidin-coated cover glass surface, and the DIG-end is attached to the antiDIG-coated superparamagnetic bead. This figure is not drawn to scale.

One shortcoming of this protocol to make torsionally constrained DNA is that the location of the labels is stochastic. A rough estimate of the number of labels on a 1 kb segment is about 6 bio-dCTPs, based on 60 C sites and the fraction of labeled nucleotides in the PCR ($\sim$1:10 labeled C to unlabeled mixed nucleotides). This can result in an uncertainty from 0 to 0.3 $\mu$m in the true contour length of the molecule being tested. For lengths greater than 10 kb ($\sim$3.4 $\mu$m), this disparity is minimal and is often ignored. If shorter labeled DNA patches were used, the uncertainty of the contour length of the molecule would be reduced. For example, incorporating multiply labeled primer oligonucleotides to the sticky end of an unlabeled DNA segment results in a torsionally constrained molecule. However, such primers are not commercially available and would be very difficult to produce ourselves. Also, smaller labeled patches make proper ligation increasingly difficult to verify. The difference in length caused by the ligation of an 18 bp DNA segment is smaller than the width of the band in agarose gel electrophoresis. It should be noted that both strands of dsDNA need not be bound multiple times, since the two strands are already held together through complementary base pairing. However, the response of the molecule to torque and stretching may differ depending on whether one or both of the strands are labeled.

# Appendix C

# Increasing the force

According to Equation 4.1, the pulling force depends on only two parameters. The properties of the magnetic field and the magnetic moment of the bead can be changed with simple adaptations to the existing equipment to increase the pulling force.

If steel wedges are attached to the magnets in the NSSN orientation, the magnetic flux will be concentrated towards the tips of the wedges. Direct analytical calculations of the expected field with the wedges in place are not possible, however, simulations were carried out using the magnetic field modeling software, Opera (Vector Fields Inc, USA). Figure C.1 shows how the field differs if the wedges are composed of air or steel. From this simulation, we notice not only an increase in the overall magnitude of the magnetic field around the tips, but also a steeper gradient. The geometry of the wedge can be optimized to generate the steepest field gradient below the wedges to yield an even stronger pulling force. The increased field strength increases the magnetic moment of the bead (if unsaturated) which also leads to a stronger force.

The second method of increasing the force is to use a bead with more ferrimagnetic material. This will increase the magnetic moment and therefore the pulling force. Commercially available beads usually contain similar concentrations of ferrimagnetic material, so the larger bead, the stronger the force available.
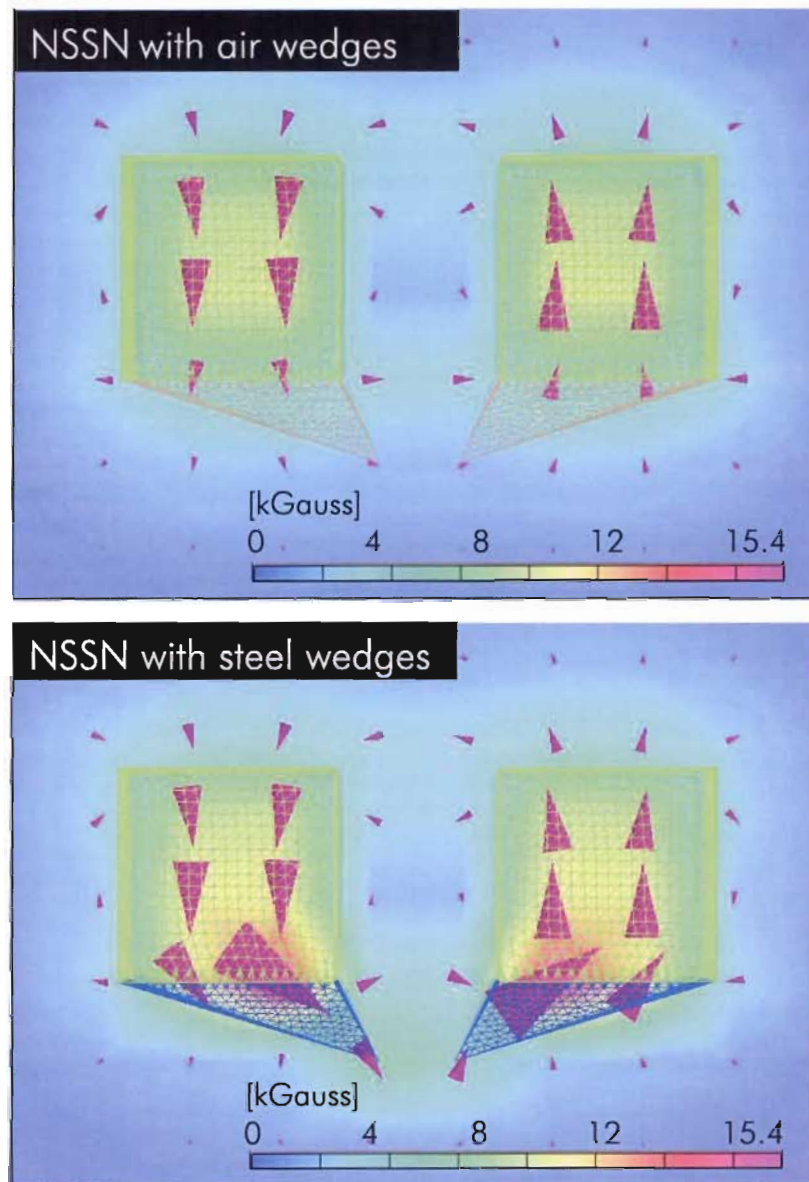
Figure C.1: The effect of adding steel wedges to the magnets on the magnetic field of the NSSN magnet orientation on the yz plane is depicted with a colour intensity map showing the intensity of $B_y$. The cones represent the direction and magnitude of the **B** field. The top portion of the figure shows the field with wedges made of air (that is, no wedges) and the bottom portion of the figure contains steel wedges. As is clearly seen, steel wedges concentrate the field towards the poles such that a stronger field and field gradient are produced below the wedge.

# Bibliography

[1] C. Bustamante, J.C. Macosko, and G.J.L. Wuite. Grabbing the cat by the tail: Manipulating molecules one by one. *Nature Reviews: Molecular Cell Biology*, 1:130–6, 2000.

[2] M.D. Stone. *Single Molecule Studies of DNA Twisting and the Mechanism of Type II Topoisomerases*. PhD thesis, University of California Berkeley, 2005.

[3] C. Haber and D. Wirtz. Magnetic tweezers for DNA micromanipulation. *Review of Scientific Instruments*, 71:4561–70, 2000.

[4] C. Gosse and V. Croquette. Magnetic tweezers: Micromanipulation and force measurement at the molecular level. *Biophysical Journal*, 82:3314–29, 2002.

[5] S. Smith, L. Finzi, and C. Bustamante. Direct mechanical measurements of the elasticity of single DNA molecules by using magnetic beads. *Science*, 258:1122–26, 1992.

[6] M. Tanase, N. Biais, and M. Sheetz. Magnetic tweezers in cell biology. *Cell Mechanics Methods in Cell Biology*, 83:473–93, 2007.

[7] J.K. Fisher *et al*. Three-dimensional force microscope: A nanometric optical tracking and magnetic manipulation system from the biomedical sciences. *Review of Scientific Instruments*, 76:053711, 2005.

[8] F. Assi, R. Jenks, J. Yang, C. Love, and M. Prentiss. Massively parallel adhesion and reactivity measurements using simple and inexpensive magnetic tweezers. *Journal of Applied Physics*, 92:5584–6, 2002.

[9] C. Danilowicz, V.W. Coljee, C Bouzigues, D.K. Lubensky, D.R. Nelson, and M. Prentiss. DNA unzipped under a constant force exhibits multiple metastable intermediates. *Proceedings of the National Academy of Sciences*, 100:1694–9, 2003.

[10] F.H.C. Crick and A.F.W. Hughes. Th physical properties of cytoplasm: A study by means of the magnetic particle method part I. experimental. *Experimental Cell Research*, 1:37–80, 1950.

[11] AR Bausch, W Moller, and E Sackmann. Measurement of local viscoelasticity and forces in living cells by magnetic tweezers. *Biophysical Journal*, 76:573–9, 1999.

[12] L. Limozin, A. Roth, and E. Sackmann. Microviscoelastic moduli of biomimetic cell envelopes. *Physical Review Letters*, 95:178101, 2005.

[13] Z. Bryant, M.D. Stone, J. Gore, S.B. Smith, N.R. Cozzarelli, and C. Bustamante. Structural transitions and elasticity from torque measurements on DNA. *Nature*, 424:338–41, 2003.

[14] A. Dawid, F. Buillemot, C. Brème, V. Croquette, and F. Heslot. Mechanically controlled DNA extrusion from a palindromic sequence by single molecule micromanipulation. *Physical Review Letters*, 96:188102, 2006.

[15] S.B. Smith, Y. Cui, and C. Bustamante. Overstretching B-DNA: The elastic response of individual double-stranded and single-stranded DNA molecules. *Science*, 271:795–9, 1996.

[16] J.A. Abels, F. Moreno-Herrero, T. van der Heijden, C. Dekker, and N.H. Dekker. Single-molecule measurements of the persistence length of double-stranded RNA. *Biophysical Journal*, 88:2737–44, 2005.

[17] T.R. Strick, J.-F. Allemand, D. Bensimon, A. Bensimon, and V. Croquette. The elasticity of a single supercoiled DNA molecule. *Science*, 271:1835–7, 1996.

[18] T. Lionnet, S. Joubaud, R. Lavery, D. Bensimon, and V. Croquette. Wringing out DNA. *Physical Review Letters*, 96:178102, 2006.

[19] J. Gore, Z. Bryant, M. Nollmann, M.U. Le, N.R. Cozzarelli, and C. Bustamante. DNA overwinds when stretched. *Nature*, 442:836–9, 2006.

[20] A. Bancaud *et al.* Structural plasticity of single chromatin fibers revealed by torsional manipulation. *Nature Structural & Molecular Biology*, 13:444–50, 2006.

[21] H. Itoh, A. Takahashi, K. Adachi, H. Noji, R. Yasuda, M. Yoshida, and K. Kinosita Jr. Mechanically driven ATP synthesis by $F_1$-ATPase. *Nature*, 427:465–8, 2004.

[22] G. Charvin, T.R. Strick, D. Bensimon, and V. Croquette. Tracking topoisomerase activity at the single-molecule level. *Annual Review Biophysics and Biomolecular Structure*, 34:201–19, 2005.

[23] J. Gore, Z. Bryant, M.D. Stone, M.N. Nollmann, N.R. Cozzarelli, and C. Bustamante. Mechanochemical analysis of DNA gyrase using rotor bead tracking. *Nature*, 439:100–4, 2006.

[24] M. Nöllmann, M.D. Stone, Z. Bryant, J. Gore, N.J. Crisona, S.C. Hong, S. Mitelheiser, A. Maxwell, C. Bustamante, and N.R. Cozzarelli. Multiple modes of *Escherichia coli* DNA gyrase activity revealed by force and torque. *Nature Structural & Molecular Biology*, 14:264–71, 2007.

[25] K.C. Neuman, T. Lionnet, and J.-F. Allemand. Single-molecule micromanipulation techniques. *Annual Review of Materials Research*, 37:33–67, 2007.

[26] T.R. Strick, J.-F. Allemand, V. Croquette, and D. Bensimon. Physical approaches to the study of DNA. *Journal of Statistical Physics*, 93:647–72, 1998.

[27] C. Bustamante, J.F. Marko, E.D. Siggia, and S. Smith. Entropic elasticity of λ-phage DNA. *Science*, 265:1599–1600, 1994.

[28] M.D. Wang, H. Yin, R. Landick, J. Gelles, and S.M. Block. Stretching DNA with optical tweezers. *Biophysical Journal*, 72:1335–46, 1997.

[29] M. Rief, H. Clausen-Schaumann, and H.E. Gaub. Sequence-dependent mechanics of single DNA molecules. *Nature Structural Biology*, 6:346–9, 1999.

[30] T.T. Perkin, D.E. Smith, R.G. Larson, and S. Chu. Stretching of a single tethered polymer in a uniform flow. *Science*, 268:83–7, 1995.

[31] E. Evans and K. Ritchie. Dynamic strength of molecular adhesion bonds. *Biophysical Journal*, 72:1541–55, 1997.

[32] D. Bensimon, A.J. Simon, V. Croquette, and A. Bensimon. Stretching DNA with a receding meniscus: Experiments and models. *Physical Review Letters*, 74:4754–7, 1995.

[33] M. Grandbois, M. Beyer, M. Rief, H. Clausen-Schaumann, and H.E. Gaub. How strong is a covalent bond? *Science*, 238:1727–30, 1999.

[34] W.A. Hendrickson, A. Pahler, J.L. Smith, Y. Satow, E.A. Merritt, and R.P. Phizackerley. Crystal structure of core streptavidin determined from multiwavelength anomalous diffraction of synchrotron radiation. *Proceedings of the National Academy of Sciences*, 7:2190–4, 1989.

[35] J. Liphardt. Personal communication (Beads/Protein G/Ab Rev.06), August 1999.

[36] P.J.M. Johnson. Toward single molecule DNA uptake by *Haemophilus influnzae*. Master's thesis, Simon Fraser University, 2007.

[37] H. Shroff, B.M. Reinhard, M. Siu, H. Agarwal, A.Spakowitz, and J. Liphart. Biocompatible force sensor with optical readout and dimensions of 6 nms$^3$, supplementary information. *Nano Letters*, 5:1509–14, 2005.

[38] A.K. Bajpai. Adsorption of bovine serum albumin onto glass powder surfaces coated with polyvinyl alcohol. *Journal of Applied Polymer Science*, 78:933–40, 2000.

[39] Invitrogen/Dynal Technical Support. Dynabeads magnetic characteristics data sheet. Technical report, 2006.

[40] C. Caizer and I. Hrianca. Dynamic magnetization of $\gamma$-Fe$_2$O$_3$ nanoparticles isolated in an SiO$_2$ amorphous matrix. *European Physical Journal B*, 31:391–400, 2003.

[41] G.E. Sommargren and H.J. Weaver. Diffraction of light by an opaque sphere. 1: Description and properties of the diffraction pattern. *Applied Optics*, 29:4646–57, 1990.

[42] G.E. Sommargren and H.J. Weaver. Diffraction of light by an opaque sphere. 2: Image formation and resolution considerations. *Applied Optics*, 31:1385–98, 1992.

[43] J.D. Jackson. *Classical Electrodynamics*. Wiley, 1999.

[44] W.J. Greenleaf, M.T. Woodside, and S.M. Block. High-resolution single-molecule measurements of biomolecular motion. *Annual Review Biophysics and Biomolecular Structure*, 36:171–90, 2007.

[45] K. Berg-Sørensen and H. Flyvbjerg. Power spectrum analysis for optical tweezers. *Review of Scientific Instruments*, 75:594–612, 2004.

[46] J.F. Allemand. *Micro-manipulations de molécules d'ADN isolées*. PhD thesis, L'université Pierre et Marie Curie, 1997.

[47] J.F. Marko and E.D. Siggia. Stretching DNA. *Macromolecules*, 28:8759–70, 1995.

[48] R.M. Robertson, S. Laib, and D.E. Smith. Diffusion of isolated DNA molecules: Dependent on length and topology. *Proceedings of the National Academy of Sciences*, 103:7319–24, 2006.

[49] T. van der Heijden, J. van Noort, H. van Leest, R. Kanaar, C. Wyman, N. Dekker, and C. Dekker. Torque-limited RecA polymerization on dsDNA. *Nucleic Acids Research*, 33:2099–105, 2005.

[50] A. Revyakin, R.H. Ebright, and T.R. Strick. Single-molecule DNA nanomanipulation: Improved resolution through use of shorter DNA fragments. *Nature Methods*, 2:127–38, 2005.